

This is a repository copy of *Oxidative desulfurization pathway for complete catabolism of sulfoquinovose by bacteria*.

White Rose Research Online URL for this paper:

<https://eprints.whiterose.ac.uk/182057/>

Version: Accepted Version

Article:

Sharma, Mahima orcid.org/0000-0003-3960-2212, Lingford, James P, Petricevic, Marija et al. (15 more authors) (2022) Oxidative desulfurization pathway for complete catabolism of sulfoquinovose by bacteria. *Proceedings of the National Academy of Sciences of the United States of America*. e2116022119. ISSN 1091-6490

<https://doi.org/10.1073/pnas.2116022119>

Reuse

Items deposited in White Rose Research Online are protected by copyright, with all rights reserved unless indicated otherwise. They may be downloaded and/or printed for private study, or other acts as permitted by national copyright laws. The publisher or other rights holders may allow further reproduction and re-use of the full text version. This is indicated by the licence information on the White Rose Research Online record for the item.

Takedown

If you consider content in White Rose Research Online to be in breach of UK law, please notify us by emailing eprints@whiterose.ac.uk including the URL of the record and the reason for the withdrawal request.

1
2 **Main Manuscript for**
3

4 **Oxidative desulfurization pathway for complete catabolism of sulfoquinovose by bacteria**
5

6 Mahima Sharma,¹ James P. Lingford,^{2,3} Marija Petricevic,^{4,5} Alexander J.D. Snow,¹ Yunyang
7 Zhang,^{4,5} Michael A. Järvå,^{2,3} Janice W.-Y. Mui,^{4,5} Nichollas E. Scott,⁶ Eleanor C. Saunders,⁷
8 Runyu Mao,^{2,3} Ruwan Epa,^{4,5} Bruna M. da Silva,^{7,8} Douglas E.V. Pires,^{7,8} David B. Ascher,^{5,7}
9 Malcolm J. McConville,⁷ Gideon J. Davies,^{1*} Spencer J. Williams,^{4,5*} Ethan D. Goddard-
10 Borger^{2,3*}
11
12

13 ¹ York Structural Biology Laboratory, Department of Chemistry, University of York, Heslington,
14 YO10 5DD, U.K.

15 ² The Walter and Eliza Hall Institute of Medical Research, Parkville, Victoria 3052, Australia.

16 ³ Department of Medical Biology, University of Melbourne, Parkville, Victoria 3010, Australia.

17 ⁴ School of Chemistry, University of Melbourne, Parkville, Victoria 3010, Australia.

18 ⁵ Bio21 Molecular Science and Biotechnology Institute, University of Melbourne, Parkville,
19 Victoria 3010, Australia

20 ⁶ Department of Microbiology and Immunology, University of Melbourne at the Peter Doherty
21 Institute for Infection and Immunity, Parkville, Victoria 3010, Australia.

22 ⁷ Department of Biochemistry and Pharmacology, Bio21 Molecular Science and Biotechnology
23 Institute, University of Melbourne, Parkville, Victoria 3010, Australia

24 ⁸ School of Computing and Information Systems, University of Melbourne, Melbourne, Victoria
25 3010, Australia
26

27 **Gideon J. Davies**

28 **Email:** gideon.davies@york.ac.uk

29 **Spencer J. Williams**

30 **Email:** sjwill@unimelb.edu.au

31 **Ethan D. Goddard-Borger**

32 **Email:** goddard-borger.e@wehi.edu.au

33

34 **Author Contributions**

35 EDG-B discovered the SMO gene cluster; SJW, EDG-B, GJD conceived project; MP and JW-YM
36 conducted microbial growth experiments; NES conducted proteomics; JPL, MS, AS, MJ performed
37 molecular biology, protein expression and structural and biophysical characterization; YZ, JPL, AS,
38 MS, RM performed biochemical assays; ECS and MJM conducted carbohydrate analysis; YZ, JW-
39 YM, BM and DA performed bioinformatics analysis; SJW, MS, EGB wrote the paper with input
40 from all authors.

41

42 **Competing Financial Interests Statement**

43 The authors declare no competing interests.

44

45 **Classification:** Physical Science/Chemistry

46 Biological Science/Biochemistry

47

48 **Keywords:** carbohydrate metabolism, sulfur cycle, oxidative desulfurization

49

50 **This PDF file includes:**

51 Main Text

52 Figures 1 to 5

53 *Abstract*

54 Catabolism of sulfoquinovose (SQ, 6-deoxy-6-sulfoglucose), the ubiquitous sulfosugar produced by
55 photosynthetic organisms, is an important component of the biogeochemical carbon and sulfur
56 cycles. Here, we describe a new pathway for SQ degradation that involves oxidative desulfurization
57 to release sulfite and enable utilization of the entire carbon skeleton of the sugar to support the
58 growth of the plant pathogen *Agrobacterium tumefaciens*. SQ or its glycoside sulfoquinovosyl
59 glycerol (SQGro) are imported into the cell by an ABC transporter system with an associated SQ
60 binding protein. A sulfoquinovosidase hydrolyses the SQ glycoside and the liberated SQ is acted on
61 by a flavin mononucleotide-dependent sulfoquinovose monooxygenase, in concert with an NADH-
62 dependent flavin reductase, to release sulfite and 6-oxo-glucose. An NADPH-dependent
63 oxidoreductase reduces the 6-oxo-glucose to glucose, enabling entry into primary metabolic
64 pathways. Structural and biochemical studies provide detailed insights into the recognition of key
65 metabolites by proteins in this pathway. Bioinformatic analyses reveal that the sulfoquinovose
66 monooxygenase (smo) pathway is distributed across Alpha- and Betaproteobacteria and is
67 especially prevalent within the Rhizobiales order. This strategy for SQ catabolism is distinct from
68 previously described pathways as it enables the complete utilization of all carbons within SQ by a
69 single organism with concomitant production of inorganic sulfite.

70

71

72 *Significance Statement*

73 Sulfoquinovose, a sulfosugar derivative of glucose, is produced by most photosynthetic organisms
74 and contains up to half of all sulfur in the biosphere. Several pathways for its breakdown are
75 known, though they provide access to only half of the carbon in sulfoquinovose and none of its
76 sulfur. Here, we describe a fundamentally different pathway within the plant pathogen
77 *Agrobacterium tumefaciens* that features oxidative desulfurization of sulfoquinovose to access all
78 carbon and sulfur within the molecule. Biochemical and structural analyses of the pathway's key
79 proteins provided insights how the sulfosugar is recognized and degraded. Genes encoding this
80 sulfoquinovose monooxygenase pathway are present in many plant pathogens and symbionts,
81 alluding to a possible role for sulfoquinovose in plant host–bacteria interactions.

82

83 **Introduction**

84 Sulfoquinovose (SQ; 6-deoxy-6-sulfoglucose) is an anionic sulfosugar found in plant and
85 cyanobacterial sulfolipids, and in S-layer proteins in archaea (1). It is estimated that SQ holds
86 around half of all sulfur in the biosphere, with 10 billion tonnes produced each year in Nature, and
87 so its cycling is a significant component of the biogeochemical sulfur cycle (2). SQ is primarily
88 found as the headgroup of the plant sulfolipid sulfoquinovosyl diacylglycerol, and its close
89 association with photosynthetic membranes and proteins supports roles in their structure and
90 function (3). Microbial communities play a dominant role in SQ cycling and usually more than one
91 organism is required to completely assimilate this source of carbon and sulfur. Organisms with a
92 tier 1 pathway, termed sulfoglycolysis, perform scission of the C3-C4 bond of SQ to give two three-
93 carbon fragments; carbons 1-3 enter central metabolism, while carbons 4-6 bearing the sulfonate are
94 excreted as dihydroxypropanesulfonate (DHPS) or sulfolactate (SL). Organisms with a tier 2
95 pathway are those that process DHPS and SL to access the remaining three carbon fragment and
96 release inorganic sulfur. To date, three tier 1 pathways have been described: the sulfoglycolytic
97 Embden-Meyerhof-Parnas (sulfo-EMP) (4), Entner-Doudoroff (sulfo-ED) (5, 6) and sulfofructose
98 transaldolase (sulfo-SFT) pathways (7, 8). Tier 2 metabolism has been described for various
99 specialized bacteria that utilize SL or DHPS and perform ‘biomineralization’ to release inorganic
100 sulfite, which under aerobic conditions is readily oxidized to sulfate (1). While many of the steps in
101 the three tier 1 sulfoglycolysis pathways differ, all three pathways share the presence of a
102 specialized glycoside hydrolase, a sulfoquinovosidase (SQase), which catalyzes the hydrolysis of
103 SQ glycosides, such as SQGro, to release SQ (9, 10).

104

105 While the tier 1 and 2 pathways described to date require two or more organisms to complete the
106 ‘biomineralization’ of SQ, there is some evidence that this can also be accomplished by a single
107 organism. Roy and co-workers have reported that an *Agrobacterium* strain from soil can completely
108 consume SQ, with release of sulfate, although the genetic and biochemical details behind this
109 process were not investigated (11). We previously reported that *A. tumefaciens* C58 contains a
110 functional SQase, with the ability to hydrolyze SQGro (9). However, analysis of its genome did not
111 reveal any genes homologous to those expected for known tier 1 sulfoglycolysis pathways.

112

113 Here, we investigate the ‘biomineralization’ of SQ by *Agrobacterium tumefaciens* (*Agrobacterium*
114 *fabrum*) strain C58 and show that this organism effects the oxidoreductive desulfurization of SQ to
115 release inorganic sulfite and glucose, which can feed into primary metabolism. We show that this
116 pathway involves: a novel SQ/SQGro solute binding protein and associated ATP-binding cassette
117 (ABC) transporter; an SQase to release SQ from its glycosides; a flavin-dependent SQ

118 monooxygenase with paired flavin-reductase to effect oxidative desulfurization of SQ to sulfite and
119 6-oxo-glucose; and a NADPH-dependent oxidoreductase to reduce 6-oxo-glucose to glucose. X-ray
120 structures determined for each of these proteins in complex with relevant metabolites reveal the
121 molecular basis of substrate binding and catalysis. We show through bioinformatics analyses that
122 this pathway – the first to enable the complete assimilation of SQ – is distributed across Alpha- and
123 Betaproteobacteria and is particularly well-represented within the Rhizobiales order.
124

125 **Results**

126 ***Differential expression of a gene cluster in the presence sulfoquinovose***

127 To determine if *A. tumefaciens* C58 can utilize SQ as a carbon source, we attempted to grow this
128 organism in M9 minimal media containing SQ as the sole carbon source. *A. tumefaciens* C58
129 exhibited robust growth in this media and analysis of spent culture supernatant failed to detect
130 DHPS or SL. Instead, the culture supernatant accumulated sulfate, but with a lag between
131 consumption of SQ and sulfate release (**Fig. 1a, Fig. S1**), as was previously reported by Roy and
132 co-workers for *Agrobacterium* sp. strain ABR2 (11). Noting that sulfite is generally released from
133 organosulfonate degradation pathways (1, 12), we analyzed the supernatant for sulfite (SO_3^{2-}), and
134 observed that SQ consumption is coincident with production of sulfite, which slowly undergoes
135 autooxidation to sulfate. To investigate the metabolism of the carbon skeleton of SQ, we cultured *A.*
136 *tumefaciens* on $^{13}\text{C}_6$ -SQ (13) and analyzed the culture supernatant using ^{13}C NMR spectroscopy
137 (**Fig. S2**). The only significant ^{13}C -labelled product we could detect was ^{13}C -bicarbonate, which
138 formed transiently during exponential phase growth, and the ^{13}C -labelled bicarbonate signal
139 disappeared at stationary phase, presumably through exchange with atmospheric CO_2 . *A.*
140 *tumefaciens* grew on other sulfoquinovosides, including SQGro and methyl α -sulfoquinovoside
141 (MeSQ), but did not grow on other alkylsulfonates including DHPS, SL, sulfoacetic acid, taurine,
142 pentanesulfonate, MES, MOPS, HEPES, PIPES, cysteic acid or methanesulfonic acid (**Fig. S3**).
143 Collectively, this data demonstrates that *A. tumefaciens* effects the complete metabolism of the
144 carbon backbone of SQ with concomitant release of sulfite.

145

146 We performed comparative proteomic experiments to identify changes associated with the growth
147 of *A. tumefaciens* on SQ compared to glucose at mid-log phase (**Fig. 1b**). The largest and most
148 significant change we observed was an increase in the abundance of proteins encoded by a single
149 cluster of genes (*Atu3277-Atu3285*) for cells grown on SQ. Proteins encoded by *Atu3283* and
150 *Atu3284* were not observed; however, they are predicted to be integral membrane proteins that can
151 be difficult to detect using conventional proteomic workflows (14). Thus, the gene cluster *Atu3277-*
152 *Atu3285*, which was subsequently renamed *smoA-smoI*, appeared to be important for growth on SQ
153 (**Fig. 1c**). While the protein encoded by *Atu3285* was previously identified as an SQase (9), the
154 proteins encoded by other genes in the cluster were not annotated with functions that were
155 consistent with any tier 1 pathway, suggesting that *A. tumefaciens* uses a different approach for the
156 catabolism of SQ. The automated annotations ascribed to the respective gene products in the
157 cluster, which included a putative ABC transporter system, sulfonate monooxygenase, SDR
158 oxidoreductase, flavin reductase and exporters, enabled development of a hypothetical biochemical
159 pathway that could explain the complete assimilation of SQ by *A. tumefaciens* (**Fig. 1d**). We

160 proceeded to biochemically validate this hypothesis and gain structural insights into the proteins
161 involved.

162

163 *Atu3282 (smoF) encodes an ABC transporter solute-binding protein that binds SQGro*

164 Within the gene cluster identified through proteomics, *Atu3281 (smoE)*, *Atu3283 (smoG)*, and
165 *Atu3284 (smoH)* were annotated as an ABC transporter system, with *Atu3282 (smoF)* encoding an
166 associated periplasmic solute-binding protein. The substrate preferences of solute binding proteins
167 are useful for assigning functions to their associated ABC transporters (15). Accordingly, we
168 produced recombinant SmoF (**Fig. S4**) and demonstrated that it binds SQGro with $K_d = 0.29 \pm 0.17$
169 μM ($\Delta H = -11 \pm 0.4 \text{ kcal mol}^{-1}$, $\Delta S = -7 \pm 2 \text{ cal mol}^{-1} \text{ deg}^{-1}$) (**Fig. 2a**, **Fig. S5**, **Table S3**). No binding
170 was observed for the stereochemically-related monosaccharides D-glucose and D-glucuronic acid.

171

172 To delineate how SmoF recognizes its ligand, we used X-ray diffraction methods to obtain a high-
173 resolution 3D structure of SmoF in its ligand-free apo state and in complex with SQGro (**Fig. 2b**,
174 **Table S4**). Like most ABC transporter solute-binding proteins, SmoF possesses two globular
175 domains with a similar α/β fold forming a deep cleft lined with aromatic and polar residues to
176 capture the ligand. Comparisons of the structures for ligand-free SmoF and the SQGro complex
177 revealed a large conformational change in the protein resulting from inter-domain rotation upon
178 SQGro binding. The relative movement of domains was assessed using the DynDom server, which
179 indicated a hinge rotation of 31° about four linker regions connecting the two domains (**Fig. S6**).
180 SQGro is buried deep within the inter-domain cleft and residues from both domains accommodate
181 this ligand through a network of hydrogen-bonding interactions (**Fig. 2c,d**). The sulfonate of
182 SQGro, which is the defining feature of this sulfosugar, is accommodated by hydrogen-bonds to the
183 side-chain of Thr220 (2.6 Å), backbone amides of Gly166 (3 Å) and Ser43 (2.8 Å), and an ordered
184 water molecule that in turn hydrogen-bonds to the sidechain of His13 (3 Å) and Gln46 (3.2 Å) (**Fig.**
185 **2c,d**). These and the other interactions in the SQGro-bound ‘closed’ state stabilized SmoF
186 substantially, as evidenced by a 15 °C increase in the protein melting temperature (**Fig. S7**).

187

188 *The structural basis of SQGro recognition by the SQase Atu3285 (SmoI)*

189 We previously reported that *Atu3285 (smoI)* encodes an SQase that preferentially hydrolyses 2'R-
190 SQGro, the natural stereoisomer of this glycoside (9). To understand the molecular basis of the
191 preference SmoI has for this stereoisomer, we determined the 3D structure of a pseudo-Michaelis
192 complex: the inactive acid/base mutant SmoI-D455N in complex with 2'R-SQGro (**Fig. 2e,f**). SmoI-
193 D455N•SQGro crystallized with four protomers in the asymmetric unit, each showing unambiguous
194 density of the substrate bound at the active site. As described previously, the overall fold is an

195 (α/β)₈ barrel appended with small β sheet domain and the sulfonate group is recognized by
196 Arg283/Trp286/Tyr491 triad⁸. Arg438 and Glu135 make hydrogen-bonding interactions with the
197 glyceryl aglycone of 2'R-SQGro. Only Arg438 interacts with the C2-hydroxyl group of the glyceryl
198 aglycone and thus this residue appears to drive selectivity for the 2'R-SQGro stereoisomer.

199
200 ***Atu3277 (smoA) encodes a flavin mononucleotide (FMN) reductase***

201 SmoA, annotated as a flavin reductase, was recombinantly expressed in *E. coli* and maintained a
202 yellow color throughout purification, suggesting that it had co-purified with a flavin co-factor. A
203 sample of this protein was heat-denatured to release the co-factor and the supernatant analyzed by
204 LC-MS to reveal that FMN was the sole detectable flavin (**Fig. S8**). Michaelis-Menten kinetics
205 were conducted for SmoA with saturating FMN and NADH or NADPH to determine which of these
206 reductants was preferred by the enzyme. With NADH the kinetic parameters were $K_M = 35 \pm 5 \mu\text{M}$,
207 $k_{\text{cat}} = 14.5 \pm 0.5 \text{ s}^{-1}$ and $k_{\text{cat}}/K_M = 4.1 \times 10^5 \text{ M}^{-1} \text{ s}^{-1}$; while for NADPH saturation was not observed and
208 $k_{\text{cat}}/K_M = 6.8 \times 10^2 \text{ M}^{-1} \text{ s}^{-1}$, indicating that NADH is the preferred cofactor for SmoA (**Fig. 3a, Fig.**
209 **S9, Fig. S10**). Owing to difficulties in obtaining structural data for this enzyme, we also studied a
210 close homologue from *Rhizobium oryzae* (*RoSmoA*, UniProt accession number: A0A1X7D6Q3),
211 which possesses a syntenic gene cluster to *Atu3277-Atu3285*. Recombinant *RoSmoA* also co-
212 purified with FMN (**Fig. S8**) and utilized the NADH cofactor with $K_M = 16 \pm 5 \mu\text{M}$, $k_{\text{cat}} = 33 \pm 2 \text{ s}^{-1}$
213 and $k_{\text{cat}}/K_M = 2.1 \times 10^6 \text{ M}^{-1} \text{ s}^{-1}$ (**Fig. S9**).

214
215 ***Atu3279 (smoC) encodes an SQ monooxygenase that desulfurizes SQ***

216 SmoC is annotated as an alkanesulfonate monooxygenase, though it possesses only 30% sequence
217 identity with the well-characterized alkanesulfonate monooxygenase SsuD, from *E. coli*. SsuD
218 catalyzes the FMNH₂- and O₂-dependent oxidation of alkanesulfonates to produce the
219 corresponding aldehyde and sulfite, with a preference for pentanesulfonate (16). The mechanism of
220 this and related enzymes have been intensively studied yet remain enigmatic. The transformation is
221 thought to involve initial formation of a C4a-peroxy or N5-peroxy flavin species on-enzyme. One
222 mechanism posits that the terminal peroxide oxygen attacks the sulfonate sulfur of the substrate
223 before undergoing a rearrangement to effect C-S bond fissure and release of the aldehyde and
224 sulfite products (**Fig. S12a**) (17). An alternative mechanism suggests the peroxide deprotonates C6,
225 which is then oxidized to an α -hydroxysulfonate that undergoes elimination to produce sulfite and
226 the aldehyde (**Fig. 12b**) (18). To demonstrate activity for recombinant SmoC (**Fig. S4**), we adapted
227 assays developed for SsuD that use Ellman's reagent to detect sulfite released by the enzyme (19).
228 Direct detection of the putative sugar product, 6-oxo-glucose (6-OG), is not trivial as this molecule
229 exists as a complex equilibrium of (hemi)acetals and hydrates that have poor stability. Thus, SmoC

230 was incubated with SQ in the presence of SmoA, FMN and NADH, which generate FMNH₂ *in situ*,
231 and the concentration of sulfite determined periodically using Ellman's reagent (**Fig. 3b**). Maximal
232 substrate conversion was approximately 200 μM (**Fig. S12c**), which is commensurate with the
233 solubility of molecular oxygen in water under standard conditions, with peak activity observed at
234 pH 8.5 (**Fig. S12d**). No activity was observed when SQ was replaced with other sulfonates,
235 including SQGro (the precursor to SQ) or HEPES (an unrelated sulfonate) demonstrating that,
236 unlike the promiscuous SsuD, SmoC has high specificity for SQ (**Fig. S12c**). As such, the
237 hydrolysis of SQGro by SmoI necessarily precedes oxidative desulfurization by SmoC. This
238 observation is further supported by ITC, where SQ was found to bind SmoC with $K_d = 3 \mu\text{M}$ in the
239 absence of any flavin-based cofactors, whereas no binding was detected for SQGro (**Fig. 3c, Fig.**
240 **S13, Table S3**). The unique SQ monooxygenase activity of SmoC defines this pathway: it is the
241 enzyme that effects fissure of the C–S bond in SQ, and so it was chosen as the namesake for this
242 gene cluster and *Atu3277-Atu3285* were renamed the **SQ MonoOxygenase** cluster (*smoA-I*).

243

244 While we could readily crystallize SmoC, these crystals only diffracted to a maximum resolution of
245 3.4 Å. The corresponding low-resolution map suggested that SmoC exists as a dimer, which was
246 confirmed in solution by SEC-MALS (**Fig. S14**). To obtain structural information for an SQ
247 monooxygenase, we turned to the homolog from *R. oryzae* (*RoSmoC*). Recombinant *RoSmoC*
248 exhibited similar activity and substrate selectivity for SQ to SmoC (**Fig. S12e**) and provided
249 crystals that diffracted to 1.9 Å. Importantly, the low-resolution structure of *A. tumefaciens* SmoC
250 superimposed with the high-resolution *RoSmoC* structures with a peptide backbone rmsd of 0.4 Å
251 across the entire structure, providing confidence that both enzymes shared a common structure and
252 function (**Fig. S15**). Both SQ monooxygenases consist of a core (α/β)₈ TIM barrel with three
253 additional insertion regions, analogous to monooxygenases from the bacterial luciferase family. The
254 protomers exist as a homodimer that buries 4697 Å² of surface area, amounting to 18% of total
255 accessible surface area for each protomer (**Fig. 3d**). Pairwise structural analysis using the DALI
256 server identified close relationships to a putative luciferase-like monooxygenase (3RAO.pdb) with
257 an rmsd of 2.4 over 314 residues and a Z score of 34.3, the FMNH₂-dependent methanesulfonate
258 monooxygenase MsuD (7K14.pdb, rmsd 2.0/322 residues, Z-score of 41.0), and the FMNH₂-
259 dependent alkanesulfonate monooxygenase SsuD (1M41.pdb, rmsd 1.8/317 residues, Z-score of
260 41.2).

261

262 Comparisons of the *RoSmoC* structure with MsuD (7K14.pdb) in complex with FMN enabled
263 identification of the FMN binding site *RoSmoC*: a deep hydrophobic pocket that accommodates
264 the isoalloxazine ring system and extends out to the protein-solvent interface, which is gated by

265 conserved phosphate-binding residues Tyr136 and Ser189 (**Fig. 3e**) (18). The close structural and
266 functional relationship of *RoSmoC* to *MsuD* is evident from the conservation of a putative sulfonate
267 binding site comprised of the side-chains Trp206, Arg236, His238, Tyr341 and His343 (18). Aside
268 from conferring these enzymes with an ability to bind sulfonates, these conserved active-site
269 residues have been suggested to contribute to the stabilization of a peroxyflavin intermediate in
270 *MsuD* and *SsuD* (18, 19). Efforts to obtain crystals of a *RoSmoC*–SQ complex were unsuccessful,
271 limiting further insights into the origin of enzyme specificity towards SQ over other sulfonates.

272

273 *Atu3278 (smoB) encodes an oxidoreductase that converts 6-oxo-glucose to glucose*

274 *SmoB* is annotated as a short-chain dehydrogenase/reductase (SDR) and we had hypothesized that it
275 was responsible for reduction of 6-OG to glucose (**Fig. 1d**). Since 6-OG is difficult to study
276 directly, we tested our hypothesis by looking for *SmoB*-mediated isotope incorporation into glucose
277 at equilibrium (**Fig. 4a**). Assuming our hypothesis to be true, and as a consequence of microscopic
278 reversibility, incubation of *SmoB* with a nicotinamide co-factor and glucose in H_2^{18}O should result
279 in transient formation of 6-OG, rapid and reversible hydration/dehydration with H_2^{18}O to compete-
280 out ^{16}O at C6 for ^{18}O , and reduction to give 6- ^{18}O -glucose. In parallel to this process, ^{18}O
281 incorporation will occur at C1 of glucose through a similar series of hydration/dehydration
282 reactions. Before proceeding with these experiments, we used ITC to establish which nicotinamide
283 cofactor was suitable for *SmoB*: NADPH bound to *SmoB* with $K_d \sim 2 \mu\text{M}$, while no binding was
284 observed for NADH (**Fig. S16, Table S3**). Thus, glucose pre-equilibrated in H_2^{18}O was incubated
285 with *SmoB* and NADP^+ then analyzed by mass spectrometry to reveal the formation of a product 4
286 Da greater in mass than glucose, presumably due to the incorporation of two ^{18}O atoms into
287 glucose. The crude reaction mixture was subjected to peracetylation (Ac_2O /pyridine) then LC-MS
288 analysis to confirm that the +4 Da product co-eluted with authentic D-glucose-pentaacetate (**Fig.**
289 **S17**). To determine that the ^{18}O label was being incorporated at C6 of glucose, we used electron-
290 impact GC-MS, which required conversion of the reaction product to the acyclic pentapropionate
291 aldonitrile (**Fig. S18**) (20). This approach provided diagnostic C1-C5 and C5-C6 fragment ions. The
292 ^{18}O -labelled product gave a C5-C6 fragment that was 2 mass units higher (m/z 173 versus 175),
293 whereas the C1-C5 fragment was the same as unlabelled glucose reference (m/z 370),
294 demonstrating that the ^{18}O is incorporated at C6. Only enzymatic reactions conducted in the
295 presence of NADP^+ produced product labelled with ^{18}O at C6: NAD^+ failed to produce any product,
296 supporting our observations by ITC and defining the cofactor specificity of *SmoB*.

297

298 We determined the 3D structure of *SmoB* using X-ray diffraction methods. This initial structure
299 revealed that *SmoB* exists as a compact trimer, however the C-terminal His₆-tag in this construct

300 occupied the putative active site of adjoining subunits, making co-crystallization with cofactors
301 difficult (**Fig. S19**). To overcome this issue, SmoB was subcloned into a different vector and
302 expressed with a cleavable N-terminal purification tag. This protein maintained the same catalytic
303 activity and SEC-MALS confirmed it remained a trimer in solution (**Fig. S20**). This SmoB
304 construct was co-crystallized with NADPH and a ternary product complex obtained by soaking
305 crystals with D-glucose (**Fig. 4b**). These crystals diffracted to a resolution of 1.5 Å and the resulting
306 model revealed that SmoB is an (α/β)₈ TIM barrel fold with a C-terminal cofactor binding site. The
307 overall fold has high structural conservation with members of the aldo-keto reductase (AKR)
308 superfamily. SmoB binds NADPH with the 2'-phosphate oxygens hydrogen-bonded to Thr284,
309 Arg289 and backbone amide of Asn285 and the adenine ring stacked between Arg289 and Phe241
310 at the C-terminus (**Fig. 4c**). NADPH binds in an extended *anti*-conformation and the nicotinamide
311 ring is located at the base of the substrate binding pocket. Trp232 makes a π - π stacking interaction
312 with the nicotinamide ring that positions the reactive center (C4) at a distance of 3 Å from C-6 of
313 glucose, appropriate for hydride transfer (**Fig. 4d**). Within the SmoB•NADP⁺•glucose complex,
314 glucose interacts with Arg152 (2.9 Å) and Lys120 (3 Å), as well as His151 (2.8 Å) and Tyr76 (2.7
315 Å) within the conserved catalytic tetrad His/Tyr/Lys/Asp that is common to the AKR superfamily
316 (**Fig. 4e**) (21).

317

318 *SMO pathways occur in the Alphaproteobacteria and Betaproteobacteria*

319 To ascertain how widespread this pathway for SQ utilization might be, a Multigene BLAST search
320 was conducted of the non-redundant protein set of the NCBI for gene clusters that contain
321 homologous SQases and SQ monooxygenases. This identified many putative *smo* gene clusters
322 across the *Agrobacterium* and *Rhizobium* genus within the *Rhizobiales* order and evidence of some
323 broader expansion into the Alphaproteobacteria and Betaproteobacteria classes (**Fig. 5**). Amongst
324 these putative *smo* gene clusters, some were syntenic while others were substantially rearranged
325 (non-syntenic) or modified to make use of other (non-ABC) transporter systems. The use of diverse
326 transport systems is not surprising: a similar phenomenon has been observed for the tier-1 sulfo-ED
327 pathway (5, 6). Indeed, sulfo-ED gene clusters have been identified in several *Rhizobiales* (5, 6),
328 suggesting that there has been ample opportunity for genetic exchanges between these pathways
329 during their evolution.

330 **Discussion**

331 While existing pathways for the breakdown of SQ require two different organisms and involve
332 scission of the carbon chain into two 3-carbon fragments, we describe here a fundamentally
333 different approach that features complete utilization of the SQ carbon skeleton. The SMO pathway
334 features several proteins with hitherto undescribed activities, including: an SQGro-binding protein;
335 an FMNH₂- and O₂-dependent SQ monooxygenase that defines this ‘SMO’ pathway by catalyzing
336 scission of the C–S bond in SQ; and an oxidoreductase dedicated to the NADPH-dependent
337 reduction of 6-OG to glucose. Like all other sulfoglycolytic pathways studied to date, the SMO
338 pathway also possesses a conserved SQase, which is essential for liberating SQ from its precursor
339 glycoside SQGro (9, 10).

340

341 The SMO pathway is reminiscent of other sugar-metabolizing pathways in bacteria. For example,
342 the SmoI (SQase), SmoF (SQGro binding protein) and SmoE/G/H (ABC transporter) proteins
343 encoded by the *smo* cluster are analogous to MalP (maltodextrin phosphorylase), MalE (maltose
344 binding protein) and MalF/G/K (ABC transporter) encoded by the *mal* operon of *E. coli* that
345 imports and degrades maltose (22). Additionally, the SmoC (SQ monooxygenase) and SmoA
346 (flavin reductase) proteins of the SMO pathway are reminiscent of the SsuD (FMNH₂-dependent
347 alkylsulfonate monooxygenase) and SsuE (NADPH-dependent FMN reductase) pair encoded by the
348 *ssu* operon of *E. coli* that degrades alkanesulfonates (16). Indeed, it is likely that the SMO pathway
349 arose through the recombination and neofunctionalization of analogous sugar- and sulfonate-
350 metabolising pathways.

351

352 Through structural analysis we identified key residues involved in sulfosugar recognition and
353 processing, in order to provide greater confidence to bioinformatic analyses of putative *smo* gene
354 clusters: an approach that has proven valuable for the identification of tier 1 sulfoglycolytic
355 pathways (9, 23, 24). This includes the Thr220-Gly166-Ser43-H₂O(His13-Gln46) cluster of SmoF
356 for the recognition of SQGro, the Arg283-Tryp286-H₂O(Tyr491) triad of SmoI for the recognition
357 of SQGro; and the Trp206-Arg236-His238-Tyr341-His343 constellation of SmoC for the
358 recognition of SQ. Given the importance of the SQ monooxygenase SmoC to the SMO pathway,
359 further empirical and computational work is warranted to understand what interactions drive its
360 selectivity for SQ, which lies in contrast with the promiscuity exhibited by alkanesulfonate
361 monooxygenases like SsuD.

362

363 The prevalence of the SMO pathway in Alphaproteobacteria of the *Rhizobiales* order is intriguing,
364 since many bacteria of this order are plant symbionts or pathogens. Indeed, those bacteria that do

365 not possess an SMO pathway often possess a complementary tier 1 sulfo-ED pathway (5).
366 Accordingly, it appears that plant sulfolipid catabolism is important for rhizobiales, whether they be
367 plant pathogens/symbionts or free-living organisms adopting an oligotrophic saprophytic lifestyle in
368 substrate replete with decaying plant tissues. Symbiotic bacteria of the *Rhizobiales* order reside
369 within the root nodules of their plant host, where they harness four-carbon substrates from the host
370 for energy and central metabolism (25). Sugawara and co-workers showed that sulfonate utilization
371 gene clusters were expressed by the plant symbiont *Bradyrhizobium diazoefficiens* USDA 110
372 within these nodules and that this may be important for utilizing diverse sulfur sources to support
373 symbiotic and possibly free-living lifestyles (26). With sulfolipid representing a large and
374 accessible pool of sulfur in plants, one possible purpose of the SMO pathway may be to salvage
375 sulfur for these bacteria. This is an important distinction between the SMO pathway and the tier 1
376 sulfoglycolytic pathways: the latter supports two-member microbial communities containing a
377 second member with a tier 2 pathway to provide access to the sulfur of SQ (27). In this sense, use of
378 the SMO pathway, which enables the complete utilization of the carbon skeleton and access to the
379 sulfur of the monosaccharide can be considered a ‘selfish’ metabolic strategy, and could provide an
380 advantage in the highly competitive soil environment or in the absence of other bacterial species
381 within colonized plant tissues. Combined with the pathway’s requirement for molecular oxygen to
382 effect C–S bond fissure, this may explain why the SMO pathway occurs within those bacteria that
383 are commonly associated with plants. Understanding how the SMO and tier 1 pathways impact
384 fitness within different environmental niches remains an important question, with answers that have
385 significant implications for understanding plant diseases and symbioses, as well as soil chemistry.
386

387 **Methods**

388 *Specialist reagents*

389 SQ and methyl α -sulfoquinovoside were purchased from MCAT GmbH (Donaueschingen,
390 Germany), ($^{13}\text{C}_6$)SQ, glycer-1-yl α -sulfoquinovoside (SQGro), and dicyclohexylammonium
391 sulfolactate, cyclohexylammonium dihydroxypropanesulfonate were synthesized as described (13,
392 28). All other sulfonates were purchased from Sigma-Aldrich.

393

394 *Growth studies*

395 Cultures of *A. tumefaciens* C58 were grown in a phosphate-buffered mineral salts media (M9, pH
396 7.2), with glucose or SQ (10 mM) as the sole carbon source. Cultures were incubated at 30 °C (250
397 rpm), with adaptation and robust growth observed within 2–3 days. These were sub-cultured (1%
398 inoculum) into the same media (10 mL) and grown at 30 °C (250 rpm). Bacterial growth was
399 quantitated using a Varian Cary50 UV/visible spectrophotometer to measure OD₆₀₀. Growth
400 experiments were replicated twice.

401

402 *Reducing sugar assay for culture supernatant*

403 The reducing sugar assay was performed according to the procedure of Blakeney and Mutton (29).
404 This assay uses pre-prepared alkaline diluent and 4-hydroxybenzoic acid hydrazide (PAHBAH)
405 working solution. Alkaline diluent was prepared by the addition of sodium hydroxide (20 g, 0.50
406 mol) to a solution of 0.10 M trisodium citrate (50 mmol, 500 mL) and 0.02 M calcium chloride (13
407 mmol, 500 mL). PAHBAH working solution was prepared by dissolving 4-hydroxybenzhydrazide
408 (PAHBAH) (0.25 g, 1.6 mmol) in alkaline diluent (50 mL). The PAHBAH working solution should
409 be made fresh shortly before use. To determine reducing sugar concentration, 0.90 mL of PAHBAH
410 working solution was added to 0.10 mL of sample. The mixture was heated at 98 °C for 4 min then
411 0.5 mL of the mixture was diluted into 1.0 mL of deionized water and the absorbance read at 415
412 nm using a Varian Cary50 UV/visible spectrophotometer. Concentrations of SQ were determined
413 with reference to a standard curve constructed using SQ.

414

415 *Turbidometric sulfate assay for culture supernatant*

416 The sulfate assay was performed according to the procedure of Sörbo (30). This assay uses a Ba-
417 PEG reagent, which contains PEG to stabilize BaSO₄ crystals and a small amount of pre-formed
418 BaSO₄ seed crystals to improve the reproducibility and linearity of the assay. The Ba-PEG reagent
419 should be prepared fresh before use. Ba-PEG reagent was prepared by dissolving BaCl₂ (42 mg,
420 0.20 mmol) and polyethylene glycol 6000 (0.75 g) in deionized water (5.0 mL). A small amount of
421 Na₂SO₄ (10 μ L, 50 mM) was added to this solution, with efficient magnetic stirring to generate

422 preformed BaSO₄ seed crystals. Individual sulfate assays were conducted as follows. An aliquot of
423 culture supernatant obtained after pelleting of cells for 5 min at 5000 g (typically 100 μL,
424 containing a maximum of 2.5 μmol of Na₂SO₄) was diluted to 0.1 mL with deionized water before
425 the addition of 0.5 M HCl (0.1 mL) followed by Ba-PEG reagent (0.1 mL). The mixture was mixed
426 vigorously and the absorbance of the sample at 400 nm determined using a Varian Cary50
427 UV/visible spectrophotometer. Concentrations of sulfate were determined by reference to a
428 standard curve constructed using Na₂SO₄. This curve was linear up to 2.5 μmol of Na₂SO₄.

429

430 *Colorimetric fuchsin sulfite assay for culture supernatant*

431 The fuchsin sulfite assay was performed according to the procedures of Brychkova *et al.* (31) and
432 Kurmanbayeva *et al.* (32). This procedure requires three pre-prepared solutions, Reagents A, B and
433 C. Reagent A was prepared by dissolution of basic fuchsin (4.0 mg, 12 μmol) in deionized water
434 (8.25 mL) at 0 °C, prior to the addition of 98% H₂SO₄ (1.25 mL). Reagent B was prepared by
435 diluting formaldehyde (36% in H₂O, 0.32 mL) in deionized water (9.68 mL) at 0°C. Reagent C was
436 prepared by dilution of Reagent A (1 mL) in deionized water (7 mL), prior to the addition of
437 solution reagent B (1 mL). Individual sulfite assays were performed by addition of Reagent C (516
438 μL) to a mixture of sample (72 μL) and 0.5 mM Na₂SO₃ (12 μL), with the latter providing a stable
439 background signal for reference. The sample was incubated at 20-22°C for 10 min and the
440 absorbance of the sample at 570 nm determined using a Varian Cary50 UV/visible
441 spectrophotometer. Concentrations of sulfite were determined by reference to a standard curve
442 constructed using Na₂SO₃.

443

444 *NMR analysis of metabolites produced from (¹³C₆)SQ*

445 M9 minimal media (5 mL) containing 10 mM glucose was inoculated with *A. tumefaciens* C58 and
446 grown to stationary phase at 30 °C (250 rpm). A 50 μL aliquot of this culture was used to inoculate
447 2 mL of M9 minimal media containing 10 mM (¹³C₆)SQ and the culture incubated at 30 °C (250
448 rpm). At OD₆₀₀ 0.27 and OD₆₀₀ 0.49, 950 μL samples of culture supernatant were diluted with 100
449 μL of D₂O and ¹³C-NMR spectra acquired using a 400 MHz spectrophotomer (100 MHz for ¹³C).

450

451 *Growth of A. tumefaciens C58 on diverse alkanesulfonates*

452 M9 minimal media (5 mL) containing 10 mM glucose was inoculated with *A. tumefaciens* C58 and
453 grown to stationary phase at 30 °C (250 rpm). A 50 μL aliquot of this starter culture was used to
454 inoculate 2 mL of M9 minimal media containing 10 mM of the alternative alkanesulfonate
455 substrate: SQ (positive control), methyl α-sulfoquinovoside (MeSQ), glycer-1-yl α-
456 sulfoquinovoside (SQGro), dicyclohexylammonium sulfolactate, cyclohexylammonium

457 dihydroxypropanesulfonate, sulfoacetic acid, taurine, sodium pentanesulfonate, cysteic acid,
458 MOPS, HEPES, PIPES, MES and methanesulfonic acid. Cultures were incubated for 30 days at 30
459 °C (250 rpm) with daily observations of optical density at 600 nm. Each experiment was performed
460 in duplicate. Growth was observed on SQ (positive control), MeSQ, and SQGro, but not on any
461 other sulfonate. Control experiments established that *A. tumefaciens* grows on glucose in the
462 presence and absence of cyclohexylamine or dicyclohexylamine, and does not grow on
463 cyclohexylamine or dicyclohexylamine alone.

464

465 *Digestion of samples for quantitative proteomics*

466 Freeze dried *A. tumefaciens* whole-cell pellets were resuspend in 500 µL lysis buffer (4% SDS, 50
467 mM Tris pH 8.5, 10 mM DTT) and boiled at 95 °C for 10 min with shaking at 2000 rpm to shear
468 DNA and inactivate protease activity. Lysates were cooled to room temperature and protein
469 concentration determined using a BCA assay. Each sample (200 µg of protein) was acetone
470 precipitated by mixing 4 volumes of ice-cold acetone with one volume of sample. Samples were
471 precipitated overnight at -20 °C and then centrifuged at 4000 × g for 10 min at 4 °C. The
472 precipitated protein pellets were resuspended with 80% ice-cold acetone and precipitated for an
473 additional 4 h at -20 °C. Samples were centrifuged at 17000 × g for 10 min at 4 °C to collect
474 precipitated protein, the supernatant was discarded and excess acetone driven off at 65 °C for 5 min.
475 Dried protein pellets were resuspended in 6 M urea, 2 M thiourea, 40 mM NH₄HCO₃ and
476 reduced/alkylated prior to digestion with Lys-C (1/200 w/w) then trypsin (1/50 w/w) overnight as
477 previously described (33). Digested samples were acidified to a final concentration of 0.5% formic
478 acid and desalted using C18 stage tips (34) before analysis by LC-MS.

479

480 *Quantitative proteomics using reversed phase LC-MS*

481 Purified peptides were resuspended in Buffer A* (2% MeCN, 0.1% TFA) and separated using a
482 Proflow-equipped Dionex Ultimate 3000 Ultra-Performance Liquid Chromatography system
483 (Thermo Fisher Scientific) with a two-column chromatography set up composed of a PepMap100
484 C18 20 mm × 75 µm trap and a PepMap C18 500 mm × 75 µm analytical column (Thermo Fisher
485 Scientific). Samples were concentrated onto the trap column at 5 µL min⁻¹ with Buffer A (2%
486 MeCN, 0.1% FA) for 6 min and then infused into an Orbitrap Q-Exactive HF Mass Spectrometer
487 (Thermo Fisher Scientific) at 250 nl min⁻¹. Peptides were separated using 124-min gradients
488 altering the buffer composition from 2% Buffer B (80% MeCN, 0.1% FA) to 8% B over 14 min,
489 then from 8% B to 30% B over 80 min, 30% B to 45% B over 10 min, 45% B to 95% B over 2 min,
490 holding at 95% B for 10, then dropped to 2% B over 1 min and holding at 2% B for the remaining 7
491 min. The Q-Exactive HF™ Mass Spectrometer was operated in a data-dependent mode

492 automatically switching between the acquisition of a single Orbitrap MS scan (120,000 resolution)
493 and a maximum of 20 MS-MS scans (HCD NCE 28, maximum fill time 40 ms, AGC 2×10^5 with a
494 resolution of 15,000).

495

496 *Mass spectrometry data analysis*

497 Proteomics datasets were searched using MaxQuant (v1.5.3.3) (35) against the *A. tumefaciens* C58
498 proteome (Uniprot proteome id UP000000813, downloaded 27/01/2018, 5344 entries). Searches
499 were performed with carbamidomethylation of cysteine set as a fixed modification and oxidation of
500 methionine as well as acetylation of protein N-termini allowed as variable modifications. The
501 protease specificity was set to trypsin allowing 2 miscleavage events with a maximum false
502 discovery rate (FDR) of 1.0% set for protein and peptide identifications. To enhance the
503 identification of peptides between samples the Match Between Runs option was enabled with a
504 precursor match window set to 2 min and an alignment window of 10 min. For label-free
505 quantitation, the MaxLFQ option within Maxquant(36) was enabled in addition to the re-
506 quantification module. The resulting protein group output was processed within the Perseus
507 (v1.4.0.6) (37) analysis environment to remove reverse matches and common protein contaminants
508 prior. For LFQ comparisons missing values were imputed using Perseus and Pearson correlations
509 visualized using R. The mass spectrometry proteomics data have been deposited to the
510 ProteomeXchange Consortium via the PRIDE (38) partner repository with the dataset identifier
511 PXD014115.

512

513 *Cloning*

514 Oligonucleotides encoding Atu3277 (SmoA), Atu3278 (SmoB), Atu3279 (SmoC) and Atu3282
515 (SmoF) were amplified by PCR using Phusion polymerase HF master mix (NEB), the appropriate
516 primers listed in **Table S1** and *A. tumefaciens* C58 gDNA as template. Oligonucleotides encoding
517 *RoSmoA* and *RoSmoC* were synthesized (IDT) to provide the sequences listed in **Table S1**. These
518 were cloned into the pET29b(+) vector at the *NdeI* and *XhoI* sites and sequence-verified by Sanger
519 sequencing to give expression vectors for SmoA, SmoB, SmoC, SmoF, *RoSmoA* and *RoSmoC*.
520 Due to interference from the SmoB C-terminal His₆-tag during structural studies, the *smoB*
521 (*Atu3278*) gene was sub-cloned into the pET-YSBLIC3C vector (39) by PCR amplification with the
522 relevant primers in **Table S1** and In-Fusion[®] cloning (Clontech Laboratories, Inc.) into linearized
523 YSBLIC3C vector according to the manufacturer's protocol. The expression plasmid was sequence-
524 verified by Sanger sequencing.

525

526 *Protein expression and purification*

527 All vectors were transformed into 'T7 Express' *E. coli* (NEB), except for the vector encoding SmoF
528 (Atu3282), which was transformed into 'Shuffle[®] T7' *E. coli* (NEB), and all were plated onto LB-
529 agar (50 $\mu\text{g mL}^{-1}$ kanamycin) and incubated at 37 °C for 16 h. A single colony was used to
530 inoculate 10 mL of LB media containing 50 $\mu\text{g mL}^{-1}$ kanamycin and the cultures incubated at 37 °C
531 for 16 h. These starter cultures were used to inoculate 1000 mL of S-broth (35 g tryptone, 20 g yeast
532 extract, 5 g NaCl, pH 7.4) containing 50 $\mu\text{g mL}^{-1}$ kanamycin, which was incubated with shaking
533 (250 rpm) at 37 °C until it reached an OD₆₀₀ of 0.8. Each culture was cooled to room temperature,
534 isopropyl thiogalactoside (IPTG) added to a final concentration of 400 μM , and incubation with
535 shaking (200 rpm) continued at 18 °C for 19 h. Cells were harvested by centrifugation at 8,000 g for
536 20 min at 4 °C then resuspended in 40 mL binding buffer (50 mM NaPi, 300 mM NaCl, 5 mM
537 imidazole, pH 7.5) containing protease inhibitor (Roche cOmplete EDTA-free protease inhibitor
538 cocktail) and lysozyme (0.1 mg mL⁻¹) by nutating at 4 °C for 30 min. Benzonase (1 μL , 250 U) was
539 added to the mixture then lysis was effected by sonication [10 \times (15 s on / 45 s off) at 45%
540 amplitude]. The lysate was centrifuged at 18,000 g for 20 min at 4 °C and the supernatant collected.
541 The supernatants were filtered (0.45 μm) and loaded onto a 1 mL HiTrap TALON IMAC column
542 (GE). The column was washed with 3 \times 10 mL of binding buffer, then the protein was eluted using
543 elution buffer (50 mM NaPi, 300 mM NaCl, 400 mM imidazole, pH 7.5). Fractions containing
544 product, as judged by SDS-PAGE, were further purified by size exclusion chromatography on a
545 HiPrep 16/60 Sephacryl S-200 HR column (GE) using 50 mM NaPi, 150 mM NaCl, pH 7.5
546 (Atu3277 SmoA; Atu3278, SmoB; Atu3279, SmoC) or 50 mM sodium citrate, 150 mM NaCl, pH
547 5.5 (Atu3282, SmoF) as buffer (**Fig. S2**). SmoI (Atu3285 or AtSQase) was prepared as previously
548 described (9).

549

550 *SEC-MALS analyses*

551 Experiments were conducted on a system comprising a Wyatt HELEOS-II multi-angle light
552 scattering detector and a Wyatt rEX refractive index detector linked to a Shimadzu LC system
553 (SPD-20A UV detector, LC20-AD isocratic pump system, DGU-20A3 degasser and SIL-20A
554 autosampler). Experiments were conducted at room temperature (20 \pm 2°C). Solvents were filtered
555 through a 0.2 μm filter prior to use and a 0.1 μm filter was present in the flow path. The column
556 was equilibrated with > 2 CV of buffer (50 mM NaPi, 300 mM NaCl pH 7.4) before use and buffer
557 was infused at the working flow rate until baselines for UV, light scattering and refractive index
558 detectors were all stable. The sample injection volume was 100 μL of protein at 6 mg mL⁻¹ in 50
559 mM NaPi buffer, 300 mM NaCl pH 7.4. Shimadzu LC Solutions software was used to control the
560 LC and Astra V software for the HELEOS-II and rEX detectors. The Astra data collection was 1
561 min shorter than the LC solutions run to maintain synchronization. Blank buffer injections were

562 used as appropriate to check for carry-over between sample runs. Data were analyzed using the
563 Astra V software. Molecular weights were estimated using the Zimm fit method with degree 1. A
564 value of 0.158 was used for protein refractive index increment (dn/dc).

565

566 *Isothermal Titration Calorimetry*

567 ITC experiments were performed using a MicroCal iTC200 (GE Healthcare) at 25 °C, with a 750
568 r.p.m. stirring speed and a reference power of 10 $\mu\text{Cal}\cdot\text{s}^{-1}$. Proteins and substrates were equilibrated
569 into degassed and filter-sterilized buffer (50 mM NaPi, 200 mM NaCl, pH 7.4 for SmoC/F and 25
570 mM NaPi, pH 7.5 for Smo B). Protein concentration was determined by BCA assay (Thermo
571 Fisher) before initiating experiments. For SmoC–SQ binding, 600 μM SQ was titrated into the ITC
572 cell containing 40 μM SmoC as a series of $10 \times 3.94 \mu\text{L}$ injections with a pre-injection of 1×0.4
573 μL . For SmoF–SQGro binding, 200 μM SQGro was titrated into the ITC cell containing 20 μM
574 SmoF as a series of $15 \times 2.94 \mu\text{L}$ injections with a pre-injection of $1 \times 0.4 \mu\text{L}$. The delay between
575 injections was set at 120 s, with an initial injection delay of 60 s. For SmoB-NAD(P)H binding, 1
576 mM NADH was titrated into the ITC cell containing 40 μM SmoB as a series of $19 \times 3 \mu\text{L}$
577 injections with a pre-injection of $1 \times 4 \mu\text{L}$. The delay between injections was set at 150 s, with an
578 initial injection delay of 180 s. All data analysis was performed in MicroCal ITC Origin Analysis
579 software (Malvern).

580

581 *Nano Differential Scanning Fluorescence analysis of SmoF*

582 Thermal stability analysis for SmoF in the presence and absence of SQGro ligand was performed on
583 a Prometheus NT.48 (NanoTemper) at 15% excitation, scanning from 20 °C to 65 °C at 0.5 °C min⁻¹.
584 All protein samples were at a concentration of 1 mg mL⁻¹ in 50 mM citrate, 150 mM NaCl at pH
585 5.5, with a 10 μL capillary load per sample. Data acquisition and analysis was performed with
586 PR.ThermControl (NanoTemper) software.

587

588 *Identification of the flavin co-factor that co-purified with SmoA*

589 100 μL of recombinant flavin reductase (SmoA or RoSmoA) at a concentration of 20 mg mL⁻¹ in 50
590 mM Tris, 150 mM NaCl, pH 8.5 was heated at 90 °C for 10 min. The sample was clarified by
591 centrifugation (16,000 $\times g$, 10 min, 4 °C) and the supernatant filtered (0.2 μm). Samples were
592 analyzed by LCMS on an Agilent LCMS system (G6125B mass detector, 1290 Infinity G7120A
593 high speed pump, 1290 Infinity G7129B autosampler, and 1290 Infinity G7117B diode array
594 detector). Conditions for LC were as follows: column: Phenomenex 00B-4752-AN Luna Omega 1.6
595 μm PS C₁₈ 100Å (50 \times 2.1 mm); injection volume: 1 μL ; gradient: 3 to 100% B over 20 min

596 (solvent A: water + 0.1% FA; solvent B: MeCN + 0.1% FA); flow rate: 0.6 mL min⁻¹; DAD – 254
597 and 214 nm.

598

599 *Michaelis-Menten kinetic analyses of SmoA and RoSmoA*

600 Reactions were conducted at 25 °C in 96-well plate format and involved the addition of SmoA or
601 *RoSmoA* (final concentration of 20 nM for NADH and 500 nM for NADPH) to 20–800 μM
602 NAD(P)H in 50 mM NaPi, 150 mM NaCl, 30 μM FMN, 0.01% BSA, pH 7.4 at a total volume of
603 100 μL. The progress of the enzyme-catalyzed conversion of NAD(P)H to NAD(P)⁺ was monitored
604 by measuring loss of absorbance at 340 nM over time using an Envision Multimodal Plate Reader
605 (Perkin Elmer). Initial rates for each reaction were calculated after first subtracting the rate of
606 spontaneous NAD(P)H oxidation (determined using an enzyme-free control) and an empirically
607 determined extinction coefficient for NAD(P)H under these conditions. Each initial rate was
608 determined in triplicate and fit to a Michaelis-Menten equation using Prism 8 (GraphPad).

609

610 *Sulfoquinovose monooxygenase assay*

611 This SQ monooxygenase activity assay is based on a previously described alkanesulfonate
612 monooxygenase activity assays (19) and uses Ellman's reagent to quantify sulfite released by these
613 enzymes. A 2 mL reaction containing 1 mM SQ, 1 mM NADH, 3 μM FMN, 0.01% (w/v) BSA, 100
614 nM SmoA or *RoSmoA* and 300 nM SQ monooxygenase (SmoC or *RoSmoC*) in buffer (25 mM Tris
615 pH 9.1, 25 mM NaCl) was incubated at 30 °C, along with controls lacking reaction components or
616 using alternate sulfonate substrates. Reactions were initiated by the addition of SmoA or *RoSmoA*
617 to the mixture. Sulfite concentration in the samples was determined at discrete time points by
618 quenching 40 μL of the reaction in 160 μL of Ellman's reagent (0.125 mg mL⁻¹ in 25 mM NaPi pH
619 7.0, prepared fresh) within a 96-well plate. After 60 s, the absorbance of the sample at 405 nm was
620 determined using an Envision Multimodal Plate Reader (Perkin Elmer). The sulfite concentration
621 was interpolated using a calibration curve generated under these conditions: a linear relationship
622 between sulfite concentration and absorbance at 405 nm was observed for 5–1000 μM Na₂SO₃. The
623 activity of SQ monooxygenases at different pH was determined by modifying the buffer in the
624 above reactions (MES: pH 6.0, 6.5 and Tris: pH 7.0, 7.5, 8.0, 8.5, 9.1) using an endpoint of $t = 30$
625 min.

626

627 *Equilibrium isotope labelling using SmoB*

628 In order to pre-label the anomeric position, glucose was incubated in 98% H₂¹⁸O with heating at 80
629 °C for 2 days, then evaporated to dryness to give C1-¹⁸O-labelled glucose. Labelling was determined
630 to be 95% by mass spectrometry based on intensities of the M and M+2 peaks. Using H₂¹⁸O buffer

631 (100 mM potassium phosphate, pH 7.0), NAD^+ and NADP^+ were each added at 0.05 molar
632 equivalent to $\text{C1-}^{18}\text{O}$ -glucose and SmoB. Four control experiments were conducted: one without
633 enzyme, one without NAD^+ and NADP^+ , one in H_2^{16}O , and one in H_2^{16}O with unlabeled glucose.
634 Reactions were monitored by mass spectrometry. Only in the experimental sample containing
635 enzyme, H_2^{18}O and $\text{NAD}^+/\text{NADP}^+$ was an M+4 signal observed and this reached a maximum
636 intensity after 72 h. Two additional reactions were performed using SmoB, glucose and either
637 NADP^+ or NAD^+ in H_2^{18}O and only the reaction containing NADP^+ generated the M+4 species. To
638 confirm that the M+4 species was glucose with two ^{18}O labels, we studied the product by HPLC.
639 However, under aqueous HPLC conditions the ^{18}O -label at C1 is lost through chemical exchange
640 with solvent. Therefore, we acetylated the product to form the pentaacetate to ensure no exchange at
641 the anomeric position during HPLC analysis. The reaction mixture from above was evaporated
642 under reduced pressure. The crude residue was treated with acetic anhydride in pyridine (1:2, 1 mL)
643 overnight. The product was extracted with EtOAc and washed with sat. CuSO_4 to remove pyridine.
644 The organic solution containing peracetylated glucose was analyzed by LCMS on an Agilent LCMS
645 system (G6125B mass detector, 1290 Infinity G7120A high speed pump, 1290 Infinity G7129B
646 autosampler, and 1290 Infinity G7117B diode array detector). Conditions for LC were as follows:
647 column: Phenomenex 00B-4752-AN Luna Omega 1.6 μm PS C_{18} 100Å (50 \times 2.1 mm); injection
648 volume: 1 μL ; gradient: 0 to 65% B over 20 min (solvent A: water + 0.1% FA; solvent B: MeCN +
649 0.1% FA); flow rate: 0.6 mL min^{-1} . Peaks with m/z 413 $[\text{M}+\text{Na}]^+$, m/z 415 $[\text{M}+2+\text{Na}]^+$, and m/z 417
650 $[\text{M}+4+\text{Na}]^+$ had the same retention time as an authentic glucose pentaacetate standard.

651

652 *GC-MS analysis of isotopically-labelled carbohydrates*

653 A 0.1 μL aliquot of SmoB-glucose reaction mixture (containing ≈ 2.5 nmol glucose) was transferred
654 to a GC vial insert (deactivated) together with 1 nmol *scyllo*-inositol as an internal standard.
655 Samples were derivatized as described in Antoniewicz *et al.* (20), with minor modifications.
656 Briefly, samples were dried (*in vacuo*, 35 $^\circ\text{C}$ with a 40 μL methanol wash), followed by addition of
657 hydroxylamine hydrochloride (20 mg mL^{-1} in 25 μL pyridine) and incubation at 90 $^\circ\text{C}$ for 1 h. Vials
658 were cooled briefly at 20-22 $^\circ\text{C}$ before the addition of propionic anhydride (50 μL) and incubation at
659 60 $^\circ\text{C}$ for 30 min. Samples were evaporated to dryness under a stream of nitrogen at 60 $^\circ\text{C}$ and
660 resuspended in EtOAc (40 μL). Control samples of $\text{U-}^{12}\text{C}$ -glucose, $\text{U-}^{13}\text{C}$ -glucose, $1,2\text{-}^{13}\text{C}_2$ -glucose
661 and $6,6\text{-}^2\text{H}_2$ -glucose were also prepared at a 2.5 nmol scale in the assay buffer mixture. Samples
662 were blinded for analysis. The derivatized labelled glucose samples (**Fig. S13** and **Table S7**) were
663 analyzed by GC-MS using a DB5 capillary column (J&W Scientific, 30 m, 250 μm inner diameter,
664 0.25 μm film thickness) with a 10 m inert duraguard. The injector insert and GC-MS transfer line
665 temperatures were 270 $^\circ\text{C}$ and 250 $^\circ\text{C}$, respectively. The oven temperature gradient was

666 programmed as follows: 70 °C (1 min); 70 °C to 295 °C at 12.5 °C min⁻¹; 295 °C to 320 °C at 25 °C
667 min⁻¹; 320 °C for 2 min. Glucose and *scyllo*-inositol were identified by reference to authentic
668 standards. A calibration curve was generated using glucose standard in assay buffer (starting
669 concentration 50 nmol, 2-fold dilution series). **Fig. S12** shows the fraction of labelled fragments,
670 corrected for isotope natural abundance by DExSI analysis (40).

671

672 *Protein crystallization*

673 Initial crystallization screening was performed using commercially available INDEX (Hampton
674 Research), PACT premier and CSSI/II (Molecular Dimensions) screens in 96-well sitting drop
675 trays. Further optimization was carried out in a 48-well sitting drop or 24-well hanging-drop format
676 to obtain optimal crystals for X-ray diffraction. Unless otherwise stated, all crystals were grown at
677 20 °C.

678

679 Crystals of apo-SmoF were obtained by mixing 0.15 µL of protein stock (50 mg mL⁻¹ protein in 50
680 mM citrate, 150 mM NaCl, pH 5.5) with 0.15 µL mother liquor (0.3 M ammonium acetate, 0.1 M
681 Bis-Tris, 25% w/v PEG 3350, pH 5.5) housed in a Rigaku Xtaltrak plate hotel to enable consistent
682 growth and monitoring at 6 °C. Crystals were harvested with nylon CryoLoopsTM (Hampton
683 Research) and cryopreserved in liquid nitrogen without additional cryoprotectants.

684

685 Crystals of SmoF were initially obtained by mixing 0.15 µL of protein stock (3.5 mg mL⁻¹ protein
686 with 2'R-SQGro at a 1:10 molar ratio in 50 mM citrate, 150 mM NaCl, pH 5.5) with 0.15 µL
687 mother liquor (30% (w/v) polyethylene glycol 4000, 0.2 M sodium acetate, 0.1 M tris chloride, pH
688 8.5). The resulting crystals were used to prepare a seed stock by mixing the crystallization drop
689 with 100 µL mother liquor and vortexing for 60 s with one teflon bead. An optimisation plate was
690 setup with drops comprised of 0.1 µl of various mother liquors (28-36% (w/v) polyethylene glycol
691 4000, 0.2 M sodium acetate, 0.1 M tris chloride, pH 7.1-9.1), 50 nl seed stock solution, and 0.15 µL
692 protein stock (4 mg mL⁻¹ protein with 2'R-SQGro at a 1:10 molar ratio in 50 mM citrate, 150 mM
693 NaCl, pH 5.5). A single crystal grown at 31.8% (w/v) polyethylene glycol 4000, 0.2 M sodium
694 acetate, 0.1 M tris chloride, pH 8.95, was harvested with a nylon CryoLoopTM (Hampton Research)
695 and cryopreserved in liquid nitrogen with 25% (v/v) ethylene glycol as cryoprotectant.

696

697 Crystals of SmoI-D455N-E370A-E371A were obtained by mixing 0.4 µL of protein stock (35 mg
698 mL⁻¹ protein in 50 mM NaPi, 300 mM NaCl, pH 7.4) with 0.5 µL mother liquor (26% PEG 3350
699 w/v, 0.2 M KSCN, 0.1 M Bis-Tris propane, pH 6.5). Crystals were soaked with solid SQGro in

700 mother liquor for 2 min prior to harvesting with nylon CryoLoopsTM (Hampton Research) and
701 cryopreserved without additional cryoprotectants.

702

703 Crystals of apo-SmoC were obtained by mixing 0.6 μL of protein stock (60 mg mL^{-1} protein in 50
704 mM Tris, 300 mM NaCl, pH 7.5) with 0.5 μL mother liquor (0.2 M NaCl, 0.1 M MES pH 6, 26%
705 PEG 6000 w/v and 10 mM SQ-glucitol). Crystals of apo-RoSmoC were obtained by mixing 0.1 μL
706 of protein stock (11.7 mg mL^{-1} protein in 50 mM Tris, 300 mM NaCl, pH 7.5) with 0.2 μL mother
707 liquor (0.2M NaNO_3 , 20% PEG 3350 w/v and 10 mM SQ). Crystals were harvested with nylon
708 CryoLoopsTM (Hampton Research) and cryopreserved in liquid nitrogen without additional
709 cryoprotectants.

710

711 Crystals of SmoB-apo (YSBLIC3C construct) were obtained by mixing 0.15 μL of protein stock
712 (20 mg mL^{-1} protein in 50 mM NaPi, 150 mM NaCl, pH 7.4) with 0.15 μL mother liquor (0.2 M
713 sodium malonate dibasic monohydrate, 0.1 M Bis-Tris propane pH 8.5, 20% w/v PEG 3350). For
714 the SmoB•NADPH complex, crystals were obtained by mixing 0.15 μL of protein stock (20 mg
715 mL^{-1} protein in 50 mM NaPi, 150 mM NaCl, 2 mM NADPH, pH 7.4) with 0.15 μL mother liquor
716 (0.1 M succinic acid, sodium dihydrogen phosphate, glycine buffer (SPG buffer, Qiagen), 25% w/v
717 PEG 1500 at pH 6.0). For the SmoB•NADPH•Glc complex, crystals were obtained in a hanging
718 drop by mixing 1 μL of protein stock (13 mg mL^{-1} protein in 50 mM NaPi 150 mM NaCl, pH 7.4)
719 with 1 μL of mother liquor (2 mM NADPH, 0.1 M SPG (Qiagen), 25% w/v PEG 1500 at pH 6).
720 Crystals were soaked with solid glucose in mother liquor for 1 min prior to harvesting with nylon
721 CryoLoopsTM (Hampton Research) and cryopreserved without additional cryoprotectants.

722

723 *X-ray data collection, processing and refinement*

724 The data were processed and integrated using XDS (41) and scaled using SCALA (42) included in
725 the Xia2 processing system (43). Data reduction was performed with AIMLESS, and resolution was
726 cut until $\text{CC1/2} = 0.5$. The structure of the SmoI•SQGro complex was determined using molecular
727 replacement using 5OHS (9) as the initial model. For SmoF, the structure was solved by molecular
728 replacement using PHASER (44) with a search model created from PDB ID: 6DTQ (45). The
729 structure of RoSmoC was solved by molecular replacement using the ensemble based on PDB ID:
730 1M41 (19) as an initial search model. The structure of SmoB was determined using molecular
731 replacement with the monomer of an aldo-keto reductase from *S. enterica* (PDB ID: 4R9O) as the
732 initial model. The apo-SmoF structure was solved using a dissected C-terminal domain of the
733 SmoF•SQGro structure. Structures were built and refined by iterative cycles using Coot (46) and
734 REFMAC (47) or Phenix (48), the latter employing local NCS restraints. Following building and

735 refinement of the protein and water molecules, clear residual density was observed in the omit maps
736 for co-complex structures, respective ligands were modelled into these. The coordinate and
737 refinement library files were prepared using ACEDRG (49). The final structures gave R_{cryst} and R_{free}
738 values along with data and refinement statistics that are presented in **Table S4-6**. Data were
739 collected at Diamond light source, Didcot, Oxfordshire, U.K., on beamlines I24 (SmoI-
740 D455N•SQGro, to 2.15 Å; SmoF-apo, to 1.88 Å), I04 (*Ro*SmoC to 1.75 Å) and I04-1 (SmoC-apo,
741 to 3.2 Å; SmoB-apo_YSB LIC3C, to 1.5 Å; SmoB-apo; pET29a; SmoB•NADPH and
742 SmoB•NADPH•Glc) and at the Australian Synchrotron using the MX2 beamline (At3282•SQGro
743 complex, to 1.7 Å). The coordinate files and structure factors have been deposited in the Protein
744 DataBank (PDB) with the coordinate accession numbers 7OFX (SmoI-D455N•SQGro), 7NBZ
745 (SmoF-apo), 7OFY (SmoF•SQGro), 7OH2 (*Ro*SmoC), 7OLF (SmoC-apo), 7BBY (SmoB-apo;
746 pET29a), 7BBZ (SmoB-apo; YSB LIC3C), 7BC0 (SmoB•NADPH) and 7BC1
747 (SmoB•NADPH•Glc).

748

749 *Structure-based analyses*

750 Crystal packing interactions were analyzed using the protein interactions, surfaces, and assemblies
751 (PISA) server (50). Structural comparisons and structure-based sequence alignments were
752 conducted using PDB25 search on DALI server against a representative subset of the Protein Data
753 Bank (51). All structure figures were generated using ccp4mg (52).

754

755 *Bioinformatic analysis SMO pathway prevalence*

756 Each gene within the *A. tumefaciens* C58 SMO gene cluster (*Atu3277-Atu3285*) was submitted as a
757 query to the NCBI BLASTp algorithm to search a database comprised of non-redundant protein
758 sequences with *A. tumefaciens* (taxid: 358) sequences excluded. Standard algorithm parameters
759 were used, except the maximum target sequences was set to 10,000. Results were filtered to only
760 retain protein sequences with E-value $\leq 1.19 \times 10^{-51}$. The corresponding nucleotide accession
761 numbers for each protein from all nine searches were extracted, combined and duplicates removed
762 to provide a list of candidate genome sequences. This was converted into a reference library for
763 MultiGeneBLAST (53) and queried using the *A. tumefaciens* C58 SMO gene cluster. Clusters
764 identified by this workflow with both an SQ monooxygenase and SQase homolog were regarded as
765 putative SMO gene clusters. Clusters representative of the observed diversity were visualized using
766 Clinker (54). A phylogenetic tree of species possessing a putative SMO gene cluster was generated
767 by pruning the All-Species Living Tree Project's 16s rRNA release 132 (55) using iTOL (56).

768

769 **Data Availability Statement**

770 Structure coordinates have been deposited in the Protein Data Bank (<https://www.rcsb.org/>) under
771 accession codes 7OFX, 7OFY, 7NBZ, 7OH2, 7OLF, 7BBZ, 7BC0, 7BC1 and 7BBY. Proteomics
772 data are available via ProteomeXchange (57) (<http://www.proteomexchange.org/>) with the identifier
773 PXD014115. Scripts used to screen for the related gene clusters listed in Figure 5 is available on
774 GitHub (<https://github.com/jmui-unimelb/Gene-Cluster-Search-Pipeline>).

775

- 777 1. E. D. Goddard-Borger, S. J. Williams Sulfoquinovose in the biosphere: occurrence,
778 metabolism and functions. *Biochem. J.* **474**, 827–849 (2017).
- 779 2. J. L. Harwood, R. G. Nicholls The plant sulpholipid - a major component of the sulphur
780 cycle. *Biochem. Soc. Trans.* **7**, 440-447 (1979).
- 781 3. N. Mizusawa, H. Wada The role of lipids in photosystem II. *Biochim. Biophys. Acta* **1817**,
782 194-208 (2012).
- 783 4. K. Denger, *et al.* Sulphoglycolysis in *Escherichia coli* K-12 closes a gap in the
784 biogeochemical sulphur cycle. *Nature* **507**, 114-117 (2014).
- 785 5. A. K. Felux, D. Spiteller, J. Klebensberger, D. Schleheck Entner-Doudoroff pathway for
786 sulfoquinovose degradation in *Pseudomonas putida* SQ1. *Proc. Natl. Acad. Sci. USA* **112**,
787 E4298-4305 (2015).
- 788 6. J. Li, *et al.* A Sulfoglycolytic Entner-Doudoroff Pathway in *Rhizobium leguminosarum* bv.
789 *trifolii* SRDI565. *Appl. Environ. Microbiol.* **86**, e00750-00720 (2020).
- 790 7. B. Frommeyer, *et al.* Environmental and Intestinal Phylum Firmicutes Bacteria Metabolize
791 the Plant Sugar Sulfoquinovose via a 6-Deoxy-6-sulfofructose Transaldolase Pathway.
792 *iScience* **23**, 101510 (2020).
- 793 8. Y. Liu, *et al.* A transaldolase-dependent sulfoglycolysis pathway in *Bacillus megaterium*
794 DSM 1804. *Biochem. Biophys. Res. Commun.* **533**, 1109-1114 (2020).
- 795 9. P. Abayakoon, *et al.* Structural and Biochemical Insights into the Function and Evolution of
796 Sulfoquinovosidases. *ACS Cent. Sci.* **4**, 1266-1273 (2018).
- 797 10. G. Speciale, Y. Jin, G. J. Davies, S. J. Williams, E. D. Goddard-Borger YihQ is a
798 sulfoquinovosidase that cleaves sulfoquinovosyl diacylglyceride sulfolipids. *Nat. Chem.*
799 *Biol.* **12**, 215-217 (2016).
- 800 11. A. B. Roy, M. J. Hewlins, A. J. Ellis, J. L. Harwood, G. F. White Glycolytic breakdown of
801 sulfoquinovose in bacteria: a missing link in the sulfur cycle. *Appl. Environ. Microbiol.* **69**,
802 6434-6441 (2003).
- 803 12. M. A. Kertesz Riding the sulfur cycle - metabolism of sulfonates and sulfate esters in Gram-
804 negative bacteria. *FEMS Microbiol. Rev.* **24**, 135-175 (2000).
- 805 13. P. Abayakoon, *et al.* Comprehensive synthesis of substrates, intermediates and products of
806 the sulfoglycolytic Embden-Meyerhoff-Parnas pathway. *J. Org. Chem.* **84**, 2901-2910
807 (2019).
- 808 14. A. E. Speers, C. C. Wu Proteomics of Integral Membrane Proteins: Theory and Application.
809 *Chem. Rev.* **107**, 3687-3714 (2007).
- 810 15. A. L. Davidson, E. Dassa, C. Orelle, J. Chen Structure, Function, and Evolution of Bacterial
811 ATP-Binding Cassette Systems. *Microbiol. Mol. Biol. Rev.* **72**, 317-364 (2008).
- 812 16. J. R. van Der Ploeg, R. Iwanicka-Nowicka, T. Bykowski, M. M. Hryniewicz, T. Leisinger
813 The *Escherichia coli* ssuEADCB gene cluster is required for the utilization of sulfur from
814 aliphatic sulfonates and is regulated by the transcriptional activator Cbl. *J. Biol. Chem.* **274**,
815 29358-29365 (1999).
- 816 17. A. Thakur, *et al.* Substrate-Dependent Mobile Loop Conformational Changes in
817 Alkanesulfonate Monooxygenase from Accelerated Molecular Dynamics. *Biochemistry* **59**,
818 3582-3593 (2020).
- 819 18. J. J. M. Liew, I. M. El Saudi, S. V. Nguyen, D. K. Wicht, D. P. Dowling Structures of the
820 alkanesulfonate monooxygenase MsuD provide insight into C-S bond cleavage, substrate
821 scope, and an unexpected role for the tetramer. *J. Biol. Chem.* **297**, (2021).
- 822 19. E. Eichhorn, C. A. Davey, D. F. Sargent, T. Leisinger, T. J. Richmond Crystal Structure of
823 *Escherichia coli* Alkanesulfonate Monooxygenase SsuD. *J. Mol. Biol.* **324**, 457-468 (2002).
- 824 20. M. R. Antoniewicz, J. K. Kelleher, G. Stephanopoulos Measuring deuterium enrichment of
825 glucose hydrogen atoms by gas chromatography/mass spectrometry. *Anal. Chem.* **83**, 3211-
826 3216 (2011).

- 827 21. T. M. Penning The aldo-keto reductases (AKRs): Overview. *Chem. Biol. Interact.* **234**, 236-
828 246 (2015).
- 829 22. R. Dippel, W. Boos The Maltodextrin System of *Escherichia coli*: Metabolism and
830 Transport. *J. Bacteriol.* **187**, 8322 (2005).
- 831 23. M. Sharma, *et al.* Dynamic Structural Changes Accompany the Production of
832 Dihydroxypropanesulfonate by Sulfolactaldehyde Reductase. *ACS Catalysis* **10**, 2826-2836
833 (2020).
- 834 24. M. Sharma, *et al.* Molecular Basis of Sulfosugar Selectivity in Sulfoglycolysis. *ACS Cent.*
835 *Sci.* **7**, 476-487 (2021).
- 836 25. M. Udvardi, P. S. Poole Transport and metabolism in legume-rhizobia symbioses. *Annu.*
837 *Rev. Plant Biol.* **64**, 781-805 (2013).
- 838 26. J. J. Speck, E. K. James, M. Sugawara, M. J. Sadowsky, P. Gyaneshwar An Alkane
839 Sulfonate Monooxygenase Is Required for Symbiotic Nitrogen Fixation by *Bradyrhizobium*
840 *diazoefficiens* (syn. *Bradyrhizobium japonicum*) USDA110(T). *Appl. Environ. Microbiol.*
841 **85**, (2019).
- 842 27. K. Denger, T. Huhn, K. Hollemeyer, D. Schleheck, A. M. Cook Sulfoquinovose degraded
843 by pure cultures of bacteria with release of C₃-organosulfonates: complete degradation in
844 two-member communities. *FEMS Microbiol. Lett.* **328**, 39-45 (2012).
- 845 28. Y. Zhang, *et al.* Concise synthesis of sulfoquinovose and sulfoquinovosyl diacylglycerides,
846 and development of a fluorogenic substrate for sulfoquinovosidases. *Org. Biomol. Chem.*
847 **18**, 675-686 (2020).
- 848 29. A. B. Blakeney, L. L. Mutton A simple colorimetric method for the determination of sugars
849 in fruit and vegetables. *J. Sci. Food Agric.* **31**, 889-897 (1980).
- 850 30. B. Sörbo (1987) Sulfate: Turbidimetric and nephelometric methods. *Methods Enzymol.*,
851 (Academic Press), Vol 143, pp 3-6.
- 852 31. G. Brychkova, D. Yarmolinsky, R. Fluhr, M. Sagi The determination of sulfite levels and its
853 oxidation in plant leaves. *Plant Sci.* **190**, 123-130 (2012).
- 854 32. A. Kurmanbayeva, *et al.* (2017) Determination of Total Sulfur, Sulfate, Sulfite, Thiosulfate,
855 and Sulfolipids in Plants. *Plant Stress Tolerance: Methods and Protocols*, ed Sunkar R
856 (Springer New York, New York, NY), pp 253-271.
- 857 33. N. E. Scott, *et al.* Simultaneous glycan-peptide characterization using hydrophilic
858 interaction chromatography and parallel fragmentation by CID, higher energy collisional
859 dissociation, and electron transfer dissociation MS applied to the N-linked glycoproteome of
860 *Campylobacter jejuni*. *Mol. Cell. Proteomics* **10**, M000031-mcp000201 (2011).
- 861 34. J. Rappsilber, M. Mann, Y. Ishihama Protocol for micro-purification, enrichment, pre-
862 fractionation and storage of peptides for proteomics using StageTips. *Nat. Protoc.* **2**, 1896-
863 1906 (2007).
- 864 35. J. Cox, M. Mann MaxQuant enables high peptide identification rates, individualized p.p.b.-
865 range mass accuracies and proteome-wide protein quantification. *Nat. Biotechnol.* **26**, 1367-
866 1372 (2008).
- 867 36. J. Cox, *et al.* Accurate Proteome-wide Label-free Quantification by Delayed Normalization
868 and Maximal Peptide Ratio Extraction, Termed MaxLFQ. *Mol. Cell. Proteomics* **13**, 2513
869 (2014).
- 870 37. S. Tyanova, *et al.* Visualization of LC-MS/MS proteomics data in MaxQuant. *Proteomics*
871 **15**, 1453-1456 (2015).
- 872 38. Y. Perez-Riverol, *et al.* The PRIDE database and related tools and resources in 2019:
873 improving support for quantification data. *Nucleic Acids Res.* **47**, D442-d450 (2019).
- 874 39. Mark J. Fogg, Anthony J. Wilkinson Higher-throughput approaches to crystallization and
875 crystal structure determination. *Biochem. Soc. Trans.* **36**, 771-775 (2008).
- 876 40. M. J. Dagley, M. J. McConville DExSI: a new tool for the rapid quantitation of ¹³C-labelled
877 metabolites detected by GC-MS. *Bioinformatics (Oxford, England)* **34**, 1957-1958 (2018).
- 878 41. W. Kabsch Xds. *Acta Crystallogr., Section D: Biol. Crystallogr.* **66**, 125-132 (2010).

- 879 42. P. Evans Scaling and assessment of data quality. *Acta Crystallogr. Sect. D* **62**, 72-82 (2006).
880 43. G. Winter xia2: an expert system for macromolecular crystallography data reduction. *J.*
881 *Appl. Crystallogr.* **43**, 186-190 (2010).
882 44. L. C. Storoni, A. J. McCoy, R. J. Read Likelihood-enhanced fast rotation functions. *Acta*
883 *Crystallogr. D Biol. Crystallogr.* **60**, 432-438 (2004).
884 45. S. Shukla, *et al.* Differential Substrate Recognition by Maltose Binding Proteins Influenced
885 by Structure and Dynamics. *Biochemistry* **57**, 5864-5876 (2018).
886 46. P. Emsley, K. Cowtan Coot: Model-building tools for molecular graphics. *Acta Crystallogr.,*
887 *Sect. D: Biol. Crystallogr.* **60**, 2126-2132 (2004).
888 47. G. N. Murshudov, A. A. Vagin, E. J. Dodson Refinement of Macromolecular Structures by
889 the Maximum-Likelihood Method. *Acta Crystallogr. Sect. D* **53**, 240-255 (1997).
890 48. P. D. Adams, *et al.* PHENIX: a comprehensive Python-based system for macromolecular
891 structure solution. *Acta Crystallogr. D Biol. Crystallogr.* **66**, 213-221 (2010).
892 49. F. Long, *et al.* AceDRG: a stereochemical description generator for ligands. *Acta*
893 *Crystallogr. Sect. D* **73**, 112-122 (2017).
894 50. E. Krissinel, K. Henrick Secondary-structure matching (SSM), a new tool for fast protein
895 structure alignment in three dimensions. *Acta Crystallogr. D* **60**, 2256-2268 (2004).
896 51. L. Holm, P. Rosenström Dali server: conservation mapping in 3D. *Nucleic Acids Res.* **38**,
897 W545-W549 (2010).
898 52. S. McNicholas, E. Potterton, K. S. Wilson, M. E. M. Noble Presenting your structures: the
899 CCP4mg molecular-graphics software. *Acta Crystallogr. D* **67**, 386-394 (2011).
900 53. M. H. Medema, E. Takano, R. Breitling Detecting sequence homology at the gene cluster
901 level with MultiGeneBlast. *Mol. Biol. Evol.* **30**, 1218-1223 (2013).
902 54. C. L. M. Gilchrist, Y. H. Chooi Clinker & clustermap.js: Automatic generation of gene
903 cluster comparison figures. *Bioinformatics (Oxford, England)*, (2021).
904 55. P. Yilmaz, *et al.* The SILVA and “All-species Living Tree Project (LTP)” taxonomic
905 frameworks. *Nucl. Acids Res.* **42**, D643-D648 (2013).
906 56. I. Letunic, P. Bork Interactive Tree Of Life (iTOL) v4: recent updates and new
907 developments. *Nucl. Acids Res.* **47**, W256-W259 (2019).
908 57. E. W. Deutsch, *et al.* The ProteomeXchange consortium in 2017: supporting the cultural
909 change in proteomics public data deposition. *Nucl. Acids Res.* **45**, D1100-D1106 (2016).

910

911

912 **Acknowledgements**

913 Dr Monica Doblin is thanked for the provision of *Agrobacterium tumefaciens* strain C58. This work
914 was supported in part by National Health and Medical Research Council of Australia (NHMRC)
915 project grants GNT1100164 (N.E.S), GNT1174405 (D.B.A.), GNT1139546 and GNT1139549
916 (E.D.G.-B); the Leverhulme Trust grant RPG-2017-190 (G.J.D.); Australian Research Council
917 grant DP180101957 and DP210100233 (S.J.W.), and DP210100362 (N.E.S.); and support from The
918 Walter and Eliza Hall Institute of Medical Research, the Australian Cancer Research Fund and a
919 Victorian State Government Operational Infrastructure support grant (E.D.G.-B). G.J.D is
920 supported by the Royal Society Ken Murray Research Professorship, E.D.G.-B. is supported by the
921 Brian M. Davis Charitable Foundation Centenary Fellowship, M.J.M. is an NHMRC Principal
922 Research Fellow, N.E.S. is supported by and Australian Research Council Future Fellowship
923 (FT200100270), B.M. was supported by Melbourne Research Scholarship, J.M. by a Sir John and
924 Lady Higgins Scholarship, M.P. by an Australian Postgraduate Award. We acknowledge Dr. Johan
925 P. Turkenburg and Sam Hart for assistance with X-ray data collection; the Diamond Light Source
926 for access to beamlines I04, i24 and I04-1 under proposal number mx-18598; and the Australian
927 Synchrotron, part of ANSTO, for access to the MX-2 beamline, which made use of the Australian
928 Cancer Research Foundation (ACRF) detector. We thank the ‘Melbourne Mass Spectrometry and
929 Proteomics Facility’ of the Bio21 Molecular Science and Biotechnology Institute at The University
930 of Melbourne for the support of mass spectrometry analysis and the ‘Bioscience Technology
931 Facility’ (University of York) for assistance with SEC-MALS analyses.

932

933 **Additional information**

934 Supplementary information

935 Correspondence should be addressed to S.J.W, G.J.D or E.D.G.-B.

936

937 **Figure 1. *A. tumefaciens* utilizes SQ and its glycosides as a carbon source.** (a) Optical density of
938 *A. tumefaciens* C58 culture (blue) and [SQ] (red), change in [sulfite] (green) and change in [sulfate]
939 (yellow), with respect to time. This data is representative of two independent experiments (see **Fig.**
940 **S1**), error bars denote observational error (derived by propagation of estimated random errors). (b)
941 Manhattan plot of comparative proteomics data for *A. tumefaciens* C58 grown on SQ vs glucose,
942 demonstrating that the most heavily upregulated proteins belong to a single gene cluster. (c) A
943 cartoon of the upregulated cluster with automated annotations for each of the gene products. These
944 would later be renamed *smoABCDEFGHI*, to reflect the importance of the sulfoquinovose
945 monooxygenase enzyme activity to this new biochemical pathway. (d) A cartoon illustrating the
946 hypothetical roles played by the gene products of this pathway to complete the catabolism of
947 SQGro.

948

949 **Figure 2. Biochemical and structural analyses of the SQGro-binding protein SmoF (Atu3282)**
950 **and SQase SmoI (Atu3285).** (a) Isothermal titration calorimogram for SmoF titrated against its
951 cognate ligand 2'R-SQGro. The data is representative of two independent experiments (see **Fig.**
952 **S5**). (b) Ribbon diagrams (with transparent surface) for the open and closed (liganded)
953 conformations of SmoF. 2'R-SQGro is bound tightly in the inter-domain cleft and is inaccessible to
954 the bulk solvent in the closed conformation. (c) Interactions between protein and ligand within the
955 SmoF•2'R-SQGro complex: SmoF is in grey, 2'R-SQGro is in green, and the 2Fo – Fc map at 1.5 σ
956 is in blue. (d) A cartoon highlighting key interactions from c. (e) Interactions between protein and
957 ligand within the complex of SmoI-D455N SQase and 2'R-SQGro: SmoI is in gold, 2'R-SQGro is
958 in green, and the 2Fo – Fc map at 1.5 σ is in blue. (f) A cartoon highlighting key interactions from e:
959 red spheres represent ordered water molecules; dotted lines represent proposed hydrogen bonds.

960

961

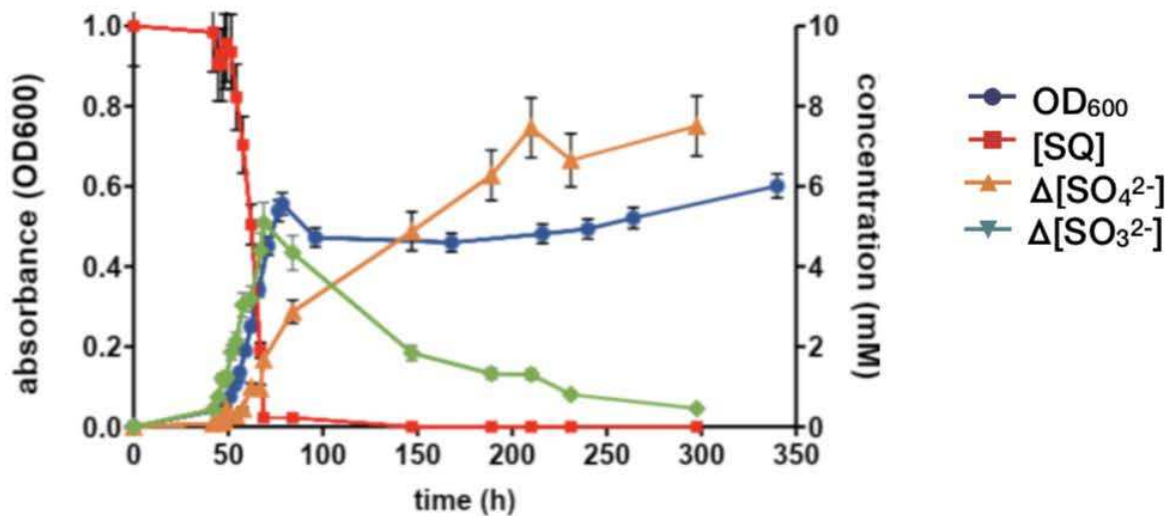
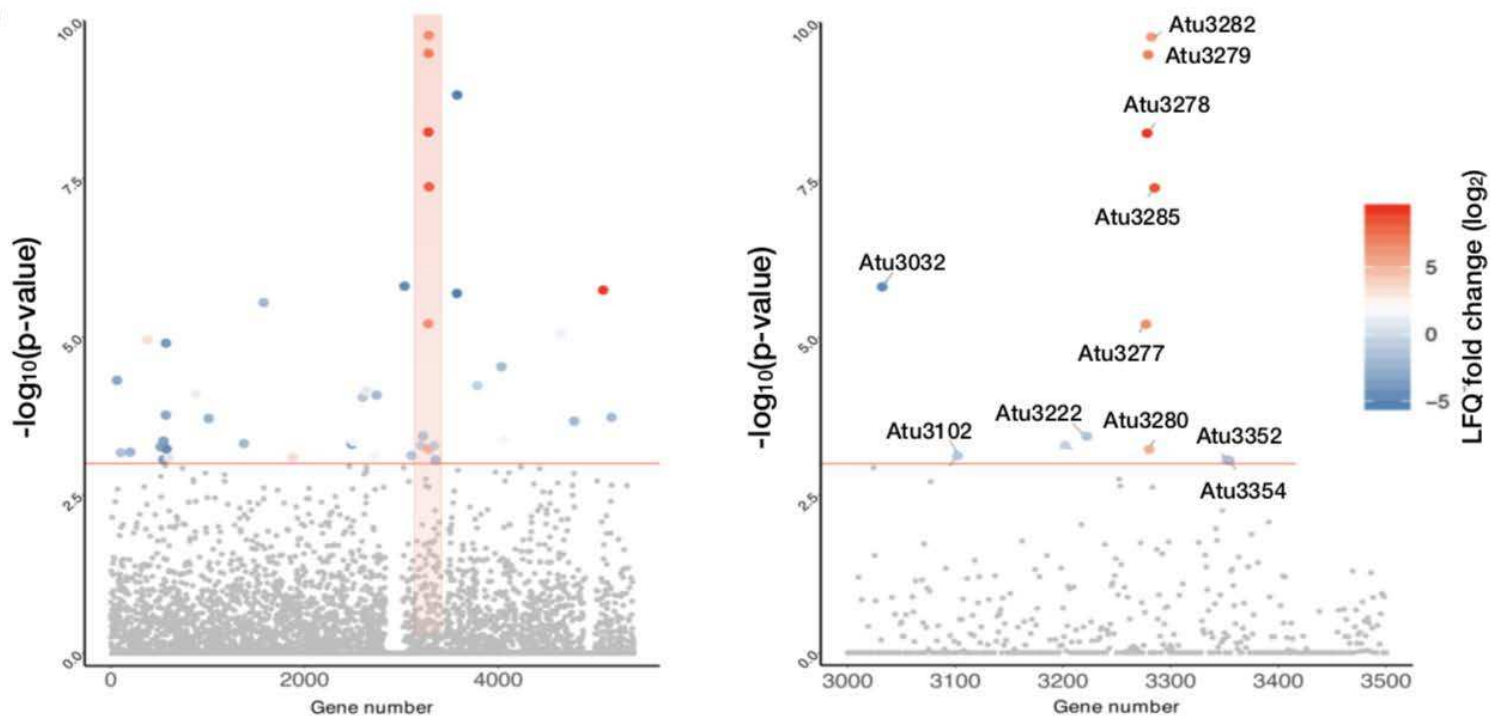
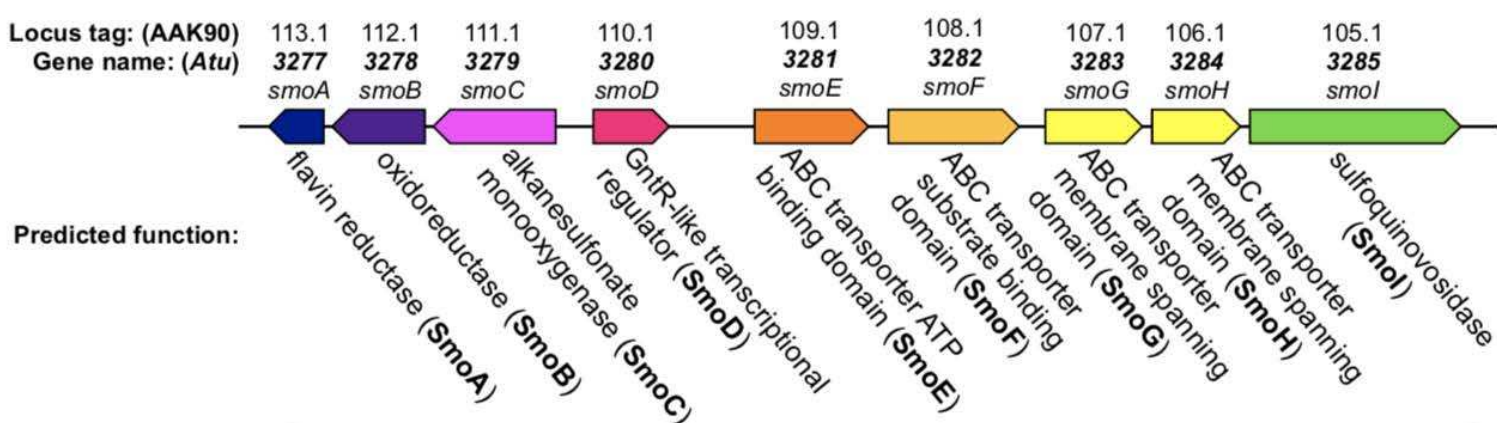
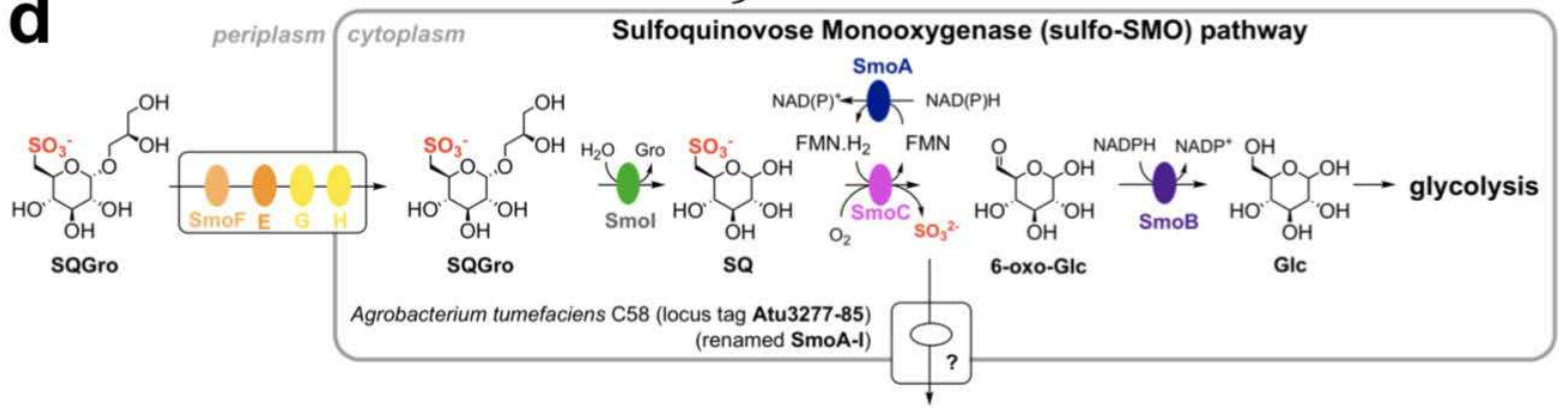
962 **Figure 3. Biochemical and structural analyses of the flavin reductase SmoA and SQ**
963 **monooxygenase SmoC.** (a) Michaelis-Menten kinetics for SmoA-catalysed reduction of FMN by
964 NADH. The data is representative of two independent replicates (see **Fig. S10**), error bars denote
965 observational errors (derived by propagation of estimated random error). (b) SmoC activity assessed
966 using sulfite release assay with Ellman's reagent in the presence of FMN, flavin reductase, NADH
967 and SQ. The data is representative of two independent experiments (see **Fig. S11**), error bars denote
968 observational error (derived by propagation of estimated random errors). (c) Isothermal titration
969 calorimogram of interaction of SmoC with SQ as determined by ITC. The data is representative of
970 two independent experiments (see **Fig. S13**). (d) Transparent molecular surface and ribbon diagram
971 of *Ro*SmoC homodimer showing cofactor binding pocket and active site (dotted circle). (e)
972 Alternative orientation of *Ro*SmoC monomer (in gold) overlaid with the MsuD·FMN·CH₃SO₃⁻
973 complex (7K14.pdb in ice blue) showing FMN from the latter. Expansion shows view of proposed
974 substrate-binding pocket and conserved residues lining the active site of *Ro*SmoC.

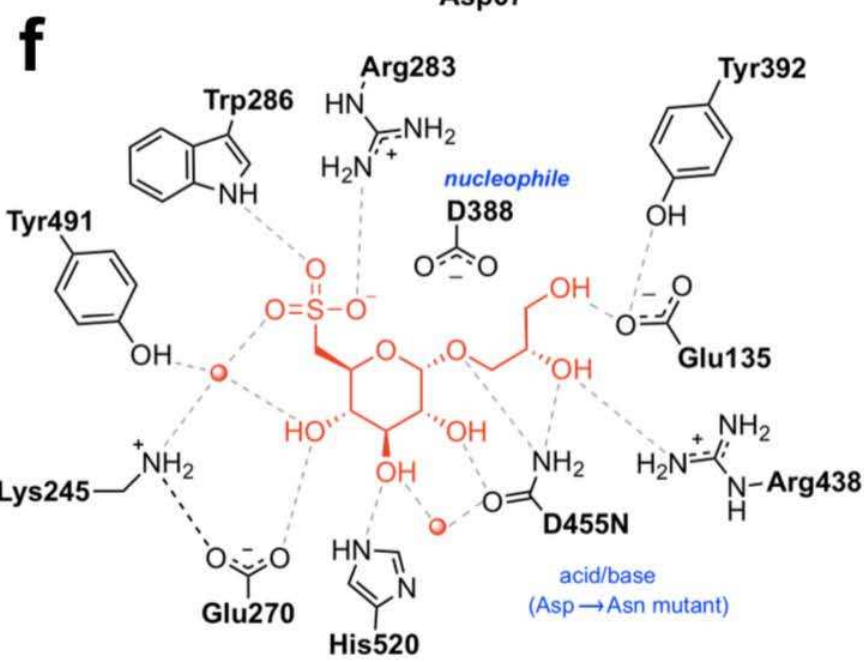
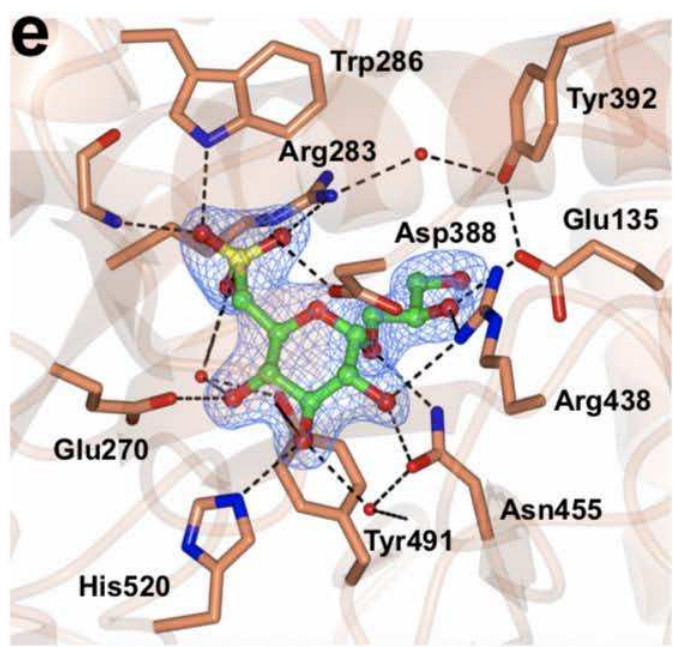
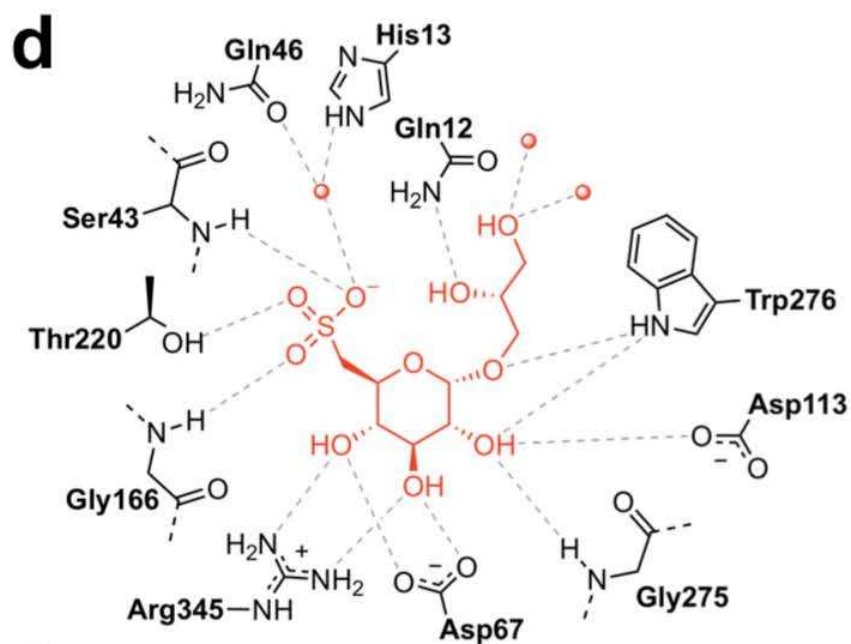
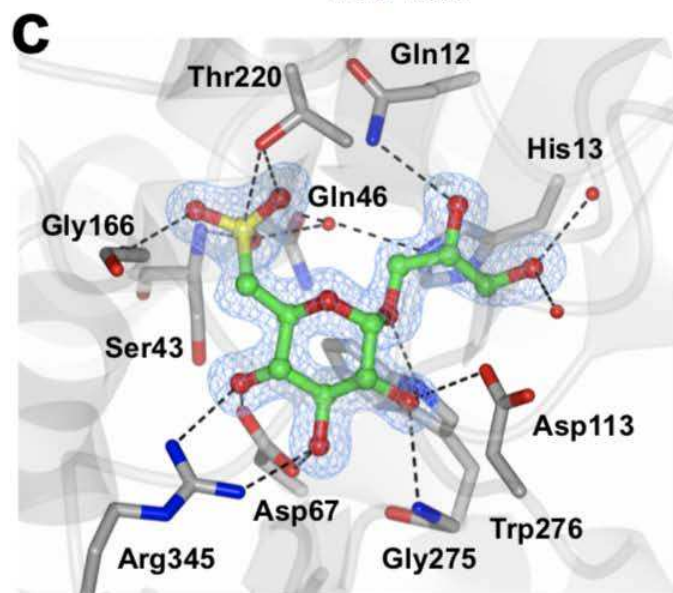
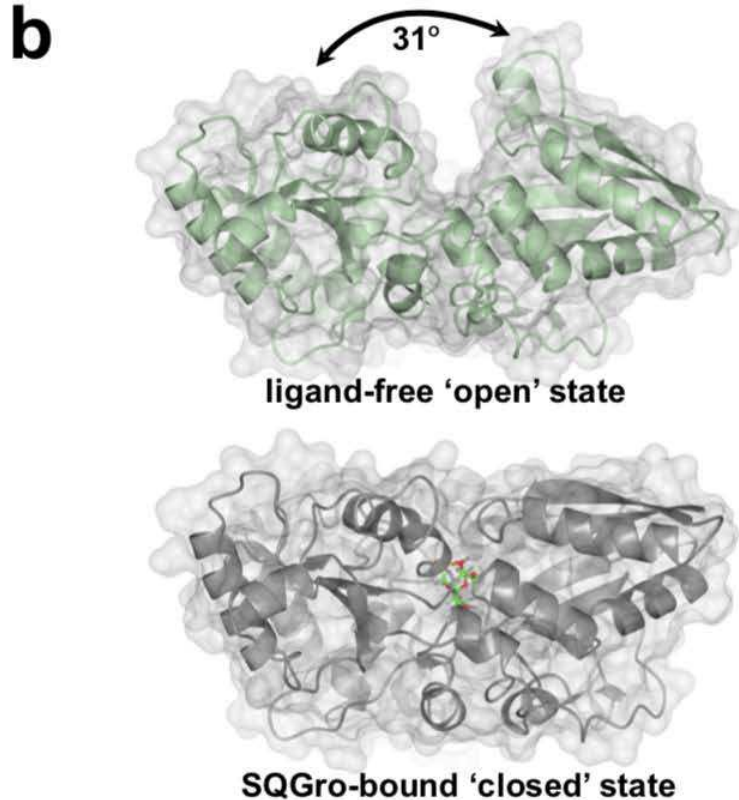
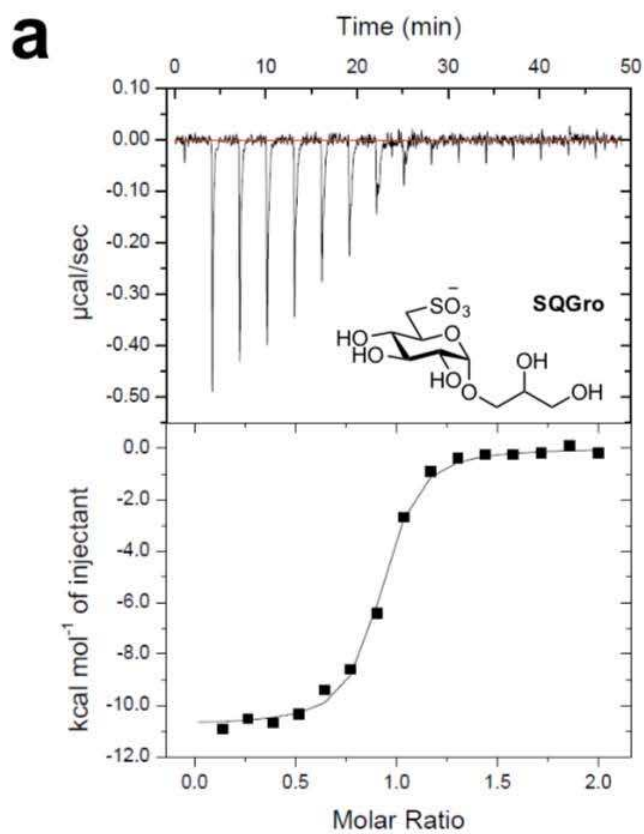
975

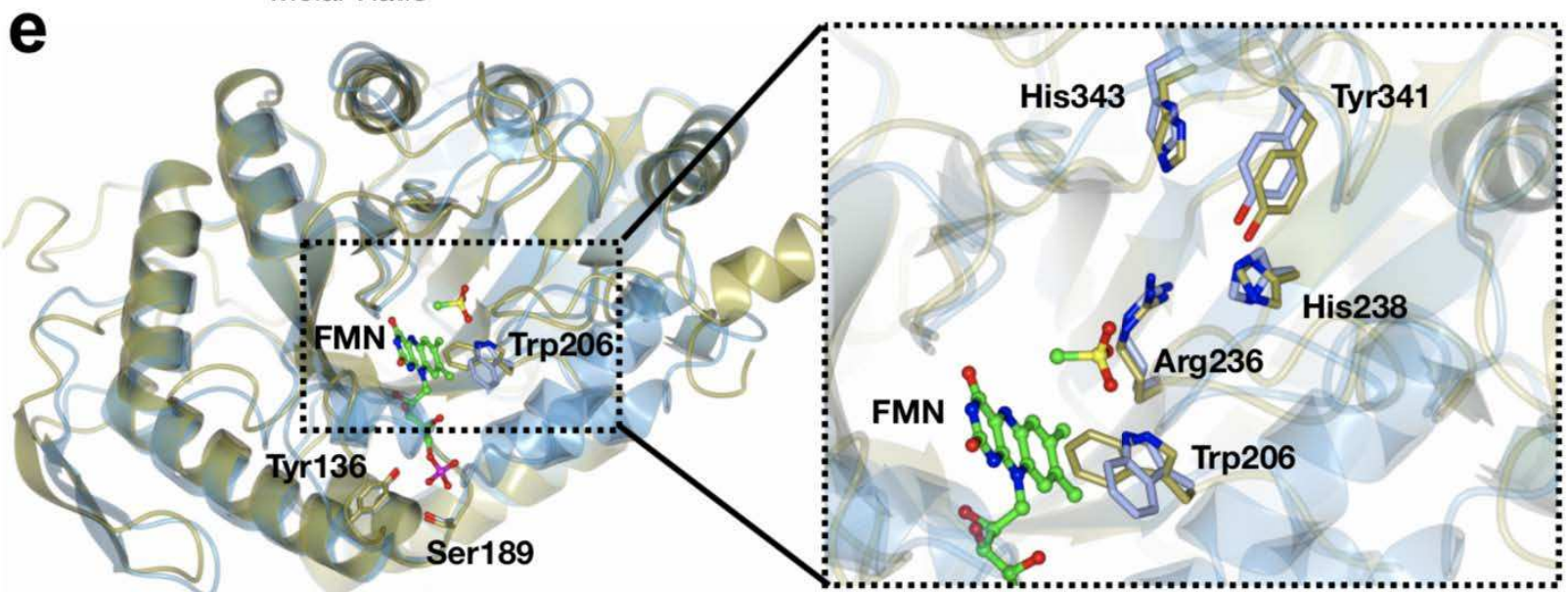
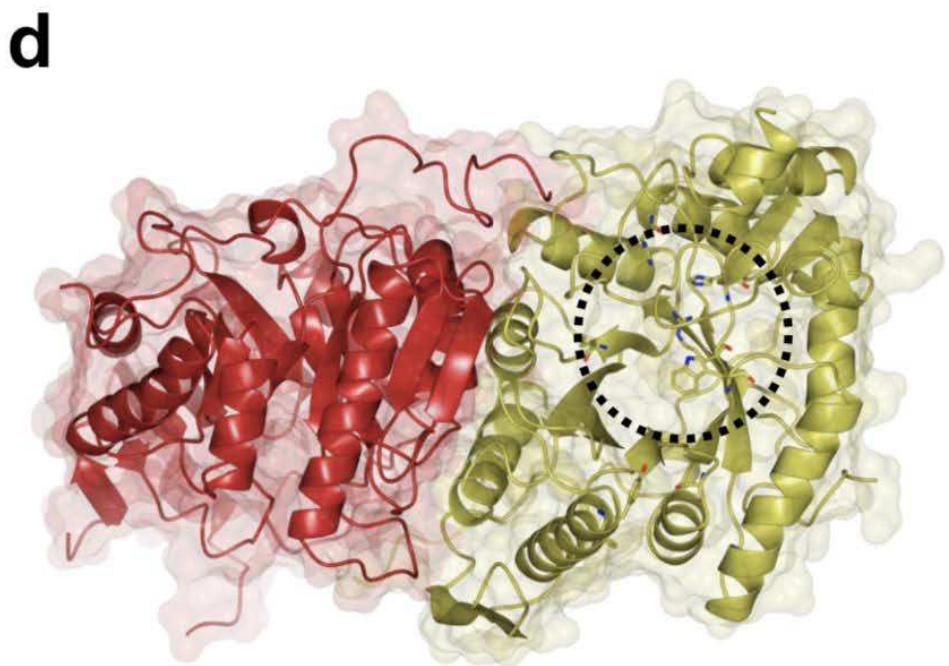
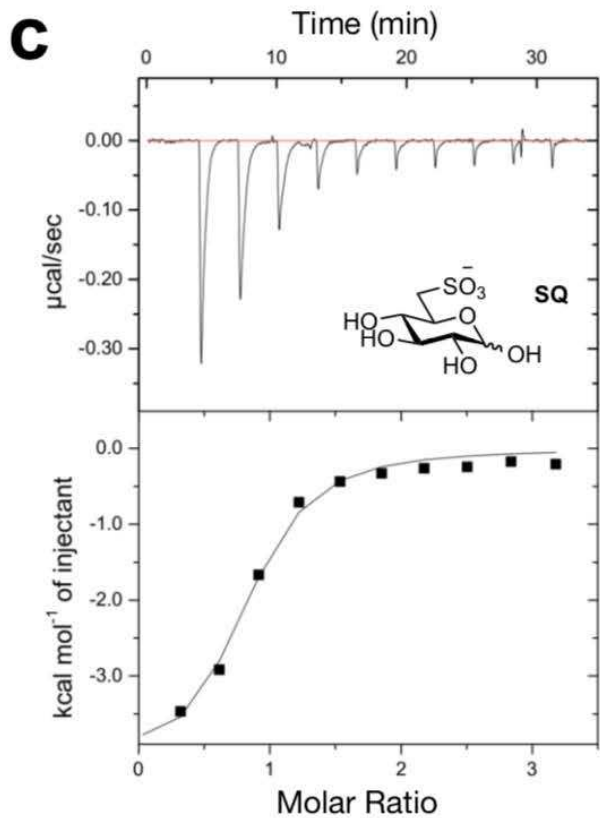
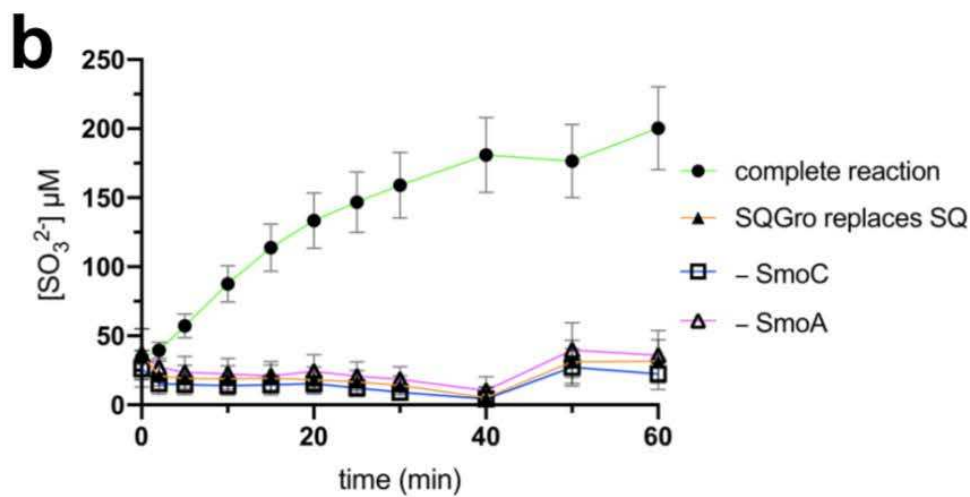
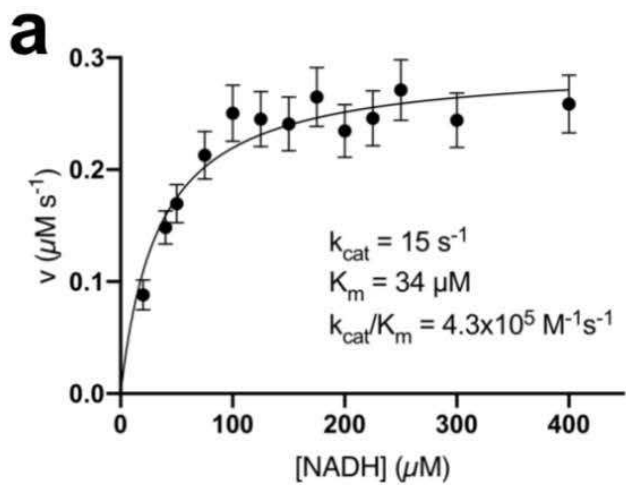
976 **Figure 4. Biochemical and structural analyses of 6-oxo-glucose reductase SmoB.** (a) Top:
977 Equilibrium oxygen exchange at C-6 of Glc via 6-OG facilitated by SmoB when incubated with
978 NADP⁺ in H₂¹⁸O. Bottom: Derivatization and MS fragmentation allows localization of ¹⁸O to C6 of
979 Glc. (b) Transparent molecular surface and ribbon diagram of SmoB in complex with NADPH and
980 Glc. (c) Closeup view of SmoB•NADPH•Glc ternary complex. Backbone and carbon atoms of
981 SmoB are shown in ice blue and NADPH and glucose are shown in cylinder format. Electron
982 density for NADPH corresponds to the 2Fo – Fc map in blue at levels of 1σ. (d) Substrate binding
983 pocket of SmoB depicting hydrogen bonding interactions of glucose with the active site residues
984 including the conserved catalytic residues Asp71, Lys 104, His151 and Tyr76. Electron density
985 corresponds to the 2Fo – Fc map (in blue) at levels of 1σ. The geometry of the SmoB-Glc complex
986 indicates the likely trajectory of hydride addition to 6-OG. (e) Proposed mechanism of SmoB
987 catalyzed reduction of 6-OG by NADPH showing hydride transfer from C4 of nicotinamide ring of
988 NADPH to C6 carbonyl and Y76 (within the catalytic tetrad) as the proton donor. The red sphere is
989 a bound water molecule; dotted lines are proposed hydrogen bonds.

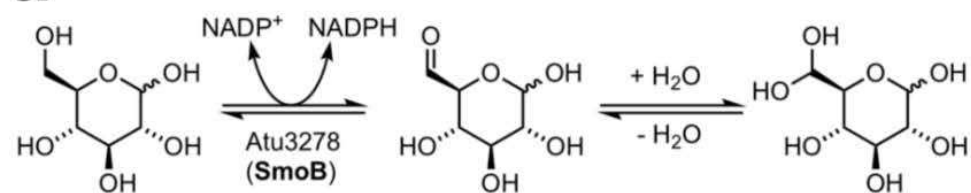
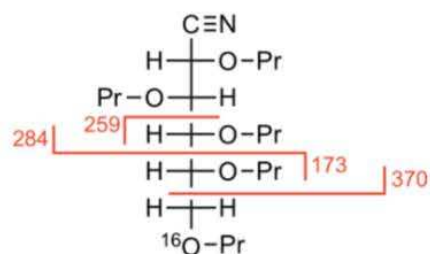
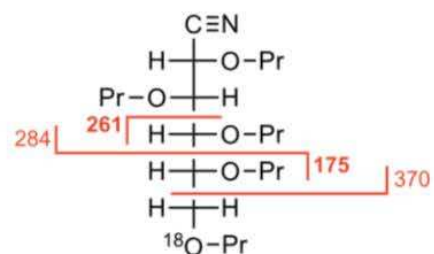
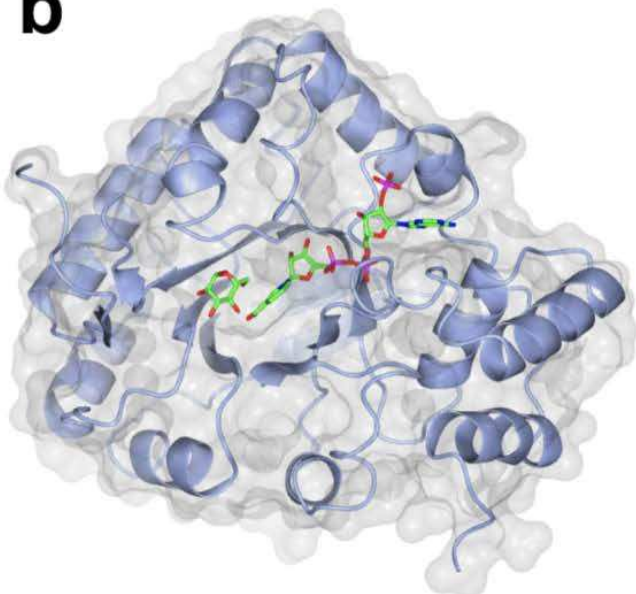
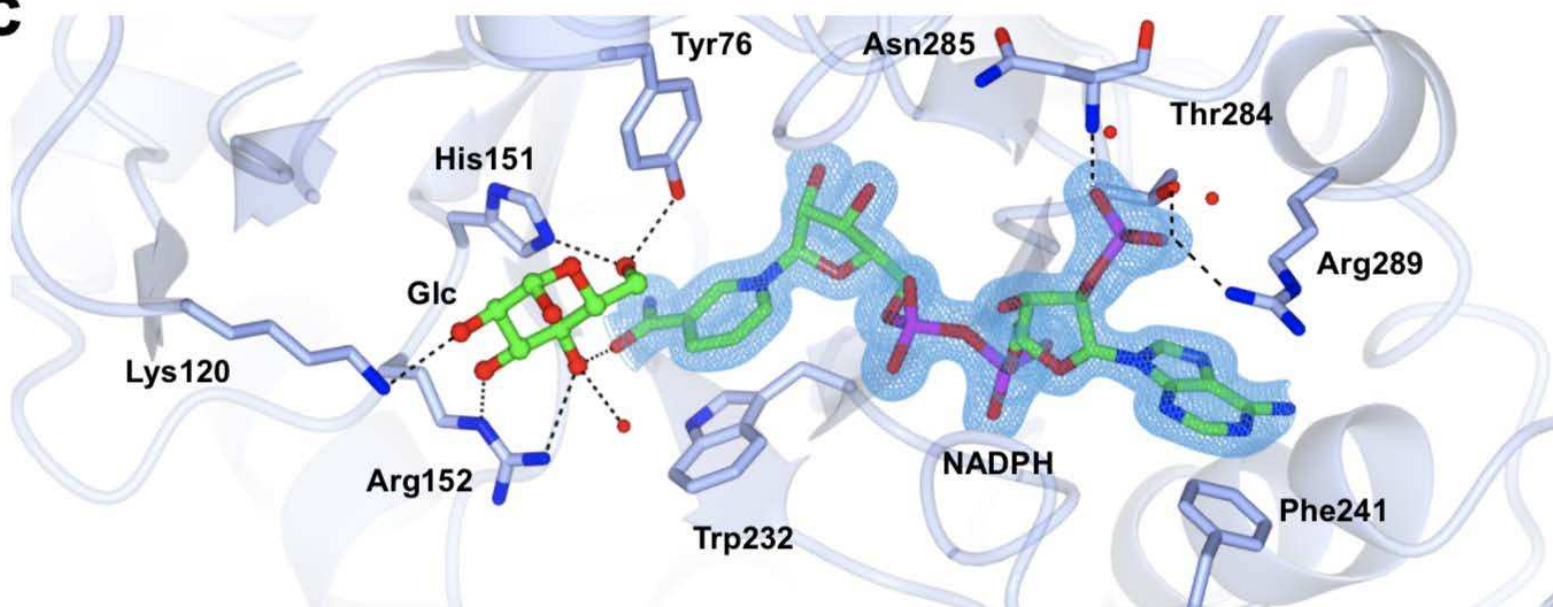
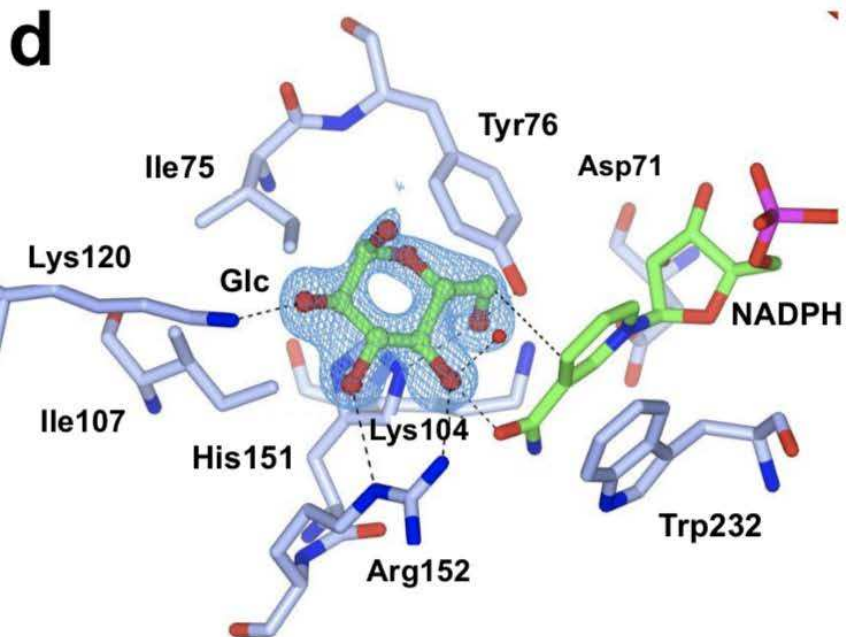
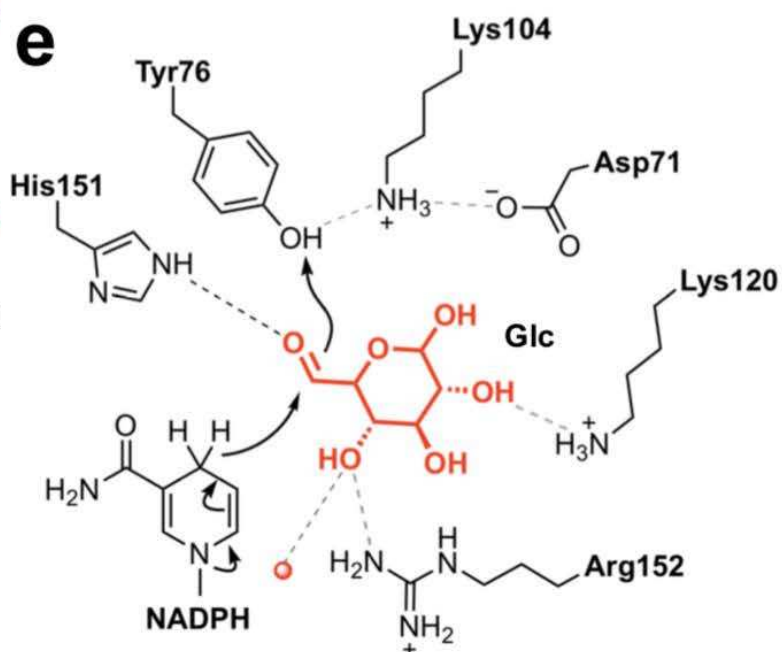
990

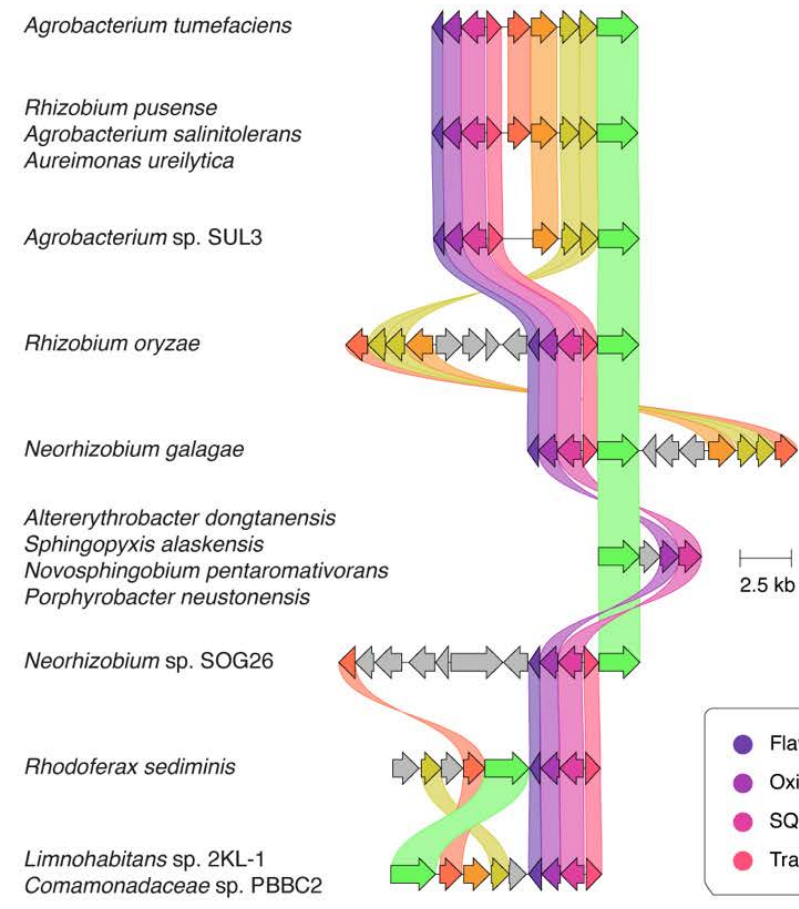
991 **Figure 5. Prevalence of the SMO pathway.** (a) Architecture of the SMO gene cluster in *A.*
992 *tumefaciens* and homologous gene clusters in other organisms. Colored links indicate $\geq 30\%$ protein
993 sequence similarity. Only those clusters encoding putative SQ monooxygenases and SQases were
994 annotated as putative SMO gene clusters. (b) A phylogenetic tree demonstrating the diversity of
995 organisms possessing putative SMO gene clusters. The tree was constructed by pruning of the All-
996 Species Living Tree Project's 16s rRNA-based LTP release 132 ([https://www.arb-](https://www.arb-silva.de/projects/living-tree/)
997 [silva.de/projects/living-tree/](https://www.arb-silva.de/projects/living-tree/)).

a**b****c****d**





a**Unlabelled sample:****C6- ^{18}O -labelled:****b****c****d****e**

a**b**